

Chiral symmetry and taste symmetry from the eigenvalue spectrum of staggered Dirac operators

Hwancheol Jeong,¹ Chulwoo Jung,² Seungyeob Jwa,¹ Jangho Kim,³ Jeehun Kim,¹ Nam Soo Kim,⁴ Sunghye Kim,¹ Sunkyu Lee,¹ Weonjong Lee,^{1,*} Youngjo Lee,⁵ and Jeonghwan Pak¹

(SWME Collaboration)

¹*Lattice Gauge Theory Research Center, FPRD, and CTP,*

Department of Physics and Astronomy, Seoul National University, Seoul 08826, South Korea

²*Physics Department, Brookhaven National Laboratory, Upton, NY11973, USA*

³*Institut für Theoretische Physik, Goethe University Frankfurt am Main,
Max-von-Laue-Str. 1, 60438 Frankfurt am Main, Germany*

⁴*Department of Electrical and Computer Engineering and the Institute of New Media and Communications
Seoul National University, Seoul 08826, South Korea*

⁵*Department of Statistics, Seoul National University, Seoul 08826, South Korea*

(Dated: May 6, 2022)

We investigate general properties of the eigenvalue spectrum for improved staggered quarks. We introduce a new chirality operator $[\gamma_5 \otimes 1]$ and a new shift operator $[1 \otimes \xi_5]$, which respect the same recursion relation as the γ_5 operator in the continuum. Then we show that matrix elements of the chirality operator sandwiched between two eigenstates of the staggered Dirac operator are related to those of the shift operator by the Ward identity of the conserved $U(1)_A$ symmetry of staggered fermion actions. We perform a numerical study in quenched QCD using HYP staggered quarks to demonstrate the Ward identity. We introduce a new concept of leakage patterns which collectively represent the matrix elements of the chirality operator and the shift operator sandwiched between two eigenstates of the staggered Dirac operator. The leakage pattern provides a new method to identify zero modes and non-zero modes in the Dirac eigenvalue spectrum. This method is as robust as the spectral flow method but requires much less computing power. Analysis using a machine learning technique confirms that the leakage pattern is universal, since the staggered Dirac eigenmodes on normal gauge configurations respect it. In addition, the leakage pattern can be used to determine a ratio of renormalization factors as a by-product. We conclude that it might be possible and realistic to measure the topological charge Q using the Atiya-Singer index theorem and the leakage pattern of the chirality operator in the staggered fermion formalism.

PACS numbers: 11.15.Ha, 12.38.Gc, 12.38.Aw

Keywords: lattice QCD, Lanczos algorithm, chiral symmetry, staggered fermion, taste symmetry

I. INTRODUCTION

It is important to understand the low-lying eigenvalue spectrum of the Dirac operator, which exhibits the topological Ward identity of the Atiya-Singer index theorem [1], the Banks-Casher relationship [2], and the universality of the distribution of the near-zero modes for fixed topological charge sectors [3, 4]. Study on the eigenvalue spectrum of the Dirac operator is, by nature, highly non-perturbative. Hence, numerical tools available in lattice gauge theory provide a perfect playground to study diverse properties of the Dirac eigenvalue spectrum.

In lattice QCD, there are a number of popular methods to implement a discrete version of the continuum Dirac operator. We are interested in one particular class of lattice fermions that are widely used in the lattice QCD community: improved staggered quarks [5–7]. Here we study the eigenvalue spectrum of staggered Dirac operators in quenched QCD to show that the small eigenvalues near zero modes of the staggered Dirac operators

reproduce the continuum properties very closely, which was originally noticed in Refs. [8–10]. To reach this conclusion, the authors of Refs. [8, 9] performed a number of tests, verifying consistency of lattice data with (1) the Atiya-Singer index theorem that describes the chiral Ward identity relating the zero modes to the topological charge; (2) the Banks-Casher relationship that relates the chiral condensate to the density of eigenvalues at the zero modes; and (3) the universality of the small eigenvalue spectrum in the ε -regime predicted by random matrix theory. In addition, the authors of Refs. [11, 12] used the spectral flow method of Adams [13] to identify the zero modes from a mixture with non-zero modes. The spectral flow method is robust but highly expensive in a computational sense.

Here, we introduce a new, advanced chirality operator $[\gamma_5 \otimes 1]$, which respects the continuum algebra of γ_5 . We show that matrix elements of this chirality operator between eigenstates are related to those of the shift operator $[1 \otimes \xi_5]$ through the Ward identity of the conserved $U(1)_A$ symmetry of staggered fermions. In addition, we introduce a new concept of leakage patterns to distinguish zero modes from non-zero modes. Using the leakage pattern of the chirality and shift operators, we show

* E-mail: wlee@snu.ac.kr

that one can measure the zero modes as reliably as when using the spectral flow method. Hence, one could determine the topological charge Q using the leakage pattern with much smaller computational cost than by using the spectral flow. We also show that it is possible to determine the ratio of renormalization constants $Z_{P \times S}/Z_{P \times P}$ using the leakage pattern.

In Section II, we briefly review the continuum theory of the eigenvalue spectrum and its relation to the quark condensate $\langle \bar{\psi}\psi \rangle$. We also review the Atiya-Singer index theorem in brief. In Section III, we briefly review the eigenvalue spectrum of staggered Dirac operators that is obtained using the Lanczos algorithm. In Section IV, we briefly review the conserved $U(1)_A$ symmetry in the staggered fermion formalism and explain its role in the eigenvalue spectrum of staggered Dirac operators. We also present numerical examples to help readers to understand basic concepts and notation. In Section V, we define the chirality operator $[\gamma_5 \otimes 1]$ and the shift operator $[1 \otimes \xi_5]$. We show that they respect the continuum recursion relation of γ_5 . Then we derive the chiral Ward identity of the $U(1)_A$ symmetry to show that the matrix elements of the chirality operator are related to those of the shift operator through the Ward identity. We discuss the eigenvalue spectrum in the continuum limit and introduce a new notation of quartet indices. Then we introduce the concept of leakage patterns for the chirality operator and the shift operator. We also present numerical examples to demonstrate that the leakage patterns of zero modes are completely different from those of non-zero modes. In Section VI, we review a machine learning technique and describe how to apply it to extract efficiently the quartet structure of non-zero modes using leakage patterns. In Section VII, we explain how the leakage pattern of the zero modes can be used to determine the ratio of the renormalization factors non-perturbatively. In Section VIII, we conclude. The appendices contain technical details on Lanczos algorithms and mathematical proofs, and more plots of leakage patterns for diverse topological charge values.

Preliminary results of this paper are published in Refs. [14–16].

II. QUARK CONDENSATE IN THE CONTINUUM

In the continuum the quark condensate is given by

$$\langle \bar{\psi}\psi \rangle = \frac{1}{N_f} \sum_f \langle 0 | \bar{\psi}_f \psi_f | 0 \rangle \quad (1)$$

$$= -\frac{1}{VN_f} \int d^4x \text{Tr} \left(\frac{1}{D+m} \right), \quad (2)$$

where D is the Dirac operator, m is the quark mass, x is the space-time coordinate, V is the volume, and N_f is the number of flavors with the same mass m . The trace is a sum over spin and color. Let us think of the

eigenvalues of the Dirac operator. D is anti-Hermitian, so its eigenvalues are purely imaginary or zero.

$$D^\dagger = -D \quad (3)$$

$$Du_\lambda(x) = i\lambda u_\lambda(x) \quad (4)$$

where λ is a real eigenvalue, and $u_\lambda(x)$ is the corresponding eigenvector.

By spectral decomposition [4],

$$\begin{aligned} S_f(x, y) &= \langle \psi_f(x) \bar{\psi}_f(y) \rangle \\ &= \sum_\lambda \frac{1}{i\lambda + m} u_\lambda(x) u_\lambda^\dagger(y) \end{aligned} \quad (5)$$

$$\langle \bar{\psi}\psi \rangle = -\frac{1}{V} \sum_\lambda \frac{1}{i\lambda + m} \int d^4x \text{Tr}(u_\lambda(x) u_\lambda^\dagger(x)) \quad (6)$$

$$= -\frac{1}{V} \sum_\lambda \frac{1}{i\lambda + m} \quad (7)$$

where we adopt the normalization convention

$$\langle u_a | u_b \rangle = \int d^4x u_a^\dagger(x) u_b(x) = \delta_{ab}. \quad (8)$$

Thanks to the chiral symmetry,

$$\gamma_5 D = -D \gamma_5 \quad (9)$$

$$D \gamma_5 | u_\lambda \rangle = -i\lambda \gamma_5 | u_\lambda \rangle \quad (10)$$

Let us define $u_{-\lambda} \equiv \gamma_5 u_\lambda$, so that $Du_{-\lambda} = -i\lambda u_{-\lambda}$. Hence, if there exists u_λ for $\lambda \neq 0$, then the parity partner eigenstate $u_{-\lambda}$ with negative eigenvalue $-i\lambda$ must also exist.

Now let us separate the zero mode contribution from the spectral decomposition.

$$\langle \bar{\psi}\psi \rangle = -\frac{1}{V} \sum_{\lambda > 0} \frac{2m}{\lambda^2 + m^2} - \frac{n_+ + n_-}{mV}. \quad (11)$$

Here, n_+ (n_-) is the number of right-handed (left-handed) zero modes per flavor. Let us define the subtracted quark condensate $\langle \bar{\psi}\psi \rangle_{\text{sub}}$:

$$\langle \bar{\psi}\psi \rangle_{\text{sub}} = \langle \bar{\psi}\psi \rangle + \frac{n_+ + n_-}{mV} = -\frac{1}{V} \sum_{\lambda > 0} \frac{2m}{\lambda^2 + m^2}. \quad (12)$$

$$= -\frac{1}{V} \sum_n \frac{2m}{\lambda_n^2 + m^2} \quad \text{with } \lambda_n > 0 \quad (13)$$

$$= -\int_{-\infty}^{+\infty} d\lambda \frac{m}{\lambda^2 + m^2} \rho_s(\lambda), \quad (14)$$

where the spectral density $\rho_s(\lambda)$ is

$$\rho_s(\lambda) = \frac{1}{V} \sum_n \delta(\lambda - \lambda_n). \quad (15)$$

Here, ρ_s is a spectral density on a single gauge configuration with volume V . Now let us average over a full ensemble of gauge field configurations and take the limit of

infinite volume ($V \rightarrow \infty$). Then, in that limit, the spectral density $\rho(\lambda) = \langle \rho_s(\lambda) \rangle$ has a well defined (smooth and continuous) value as $\lambda \rightarrow 0$. We can define the chiral condensate as

$$\begin{aligned} \Sigma &= -\langle 0 | \bar{\psi} \psi | 0 \rangle_{\text{sub}}(m=0) \\ &= \lim_{m \rightarrow 0} \int_{-\infty}^{+\infty} d\lambda \frac{m}{\lambda^2 + m^2} \rho(\lambda) = \pi \rho(0), \end{aligned} \quad (16)$$

which is the Banks-Casher relation. The subtracted quark condensate $\langle \bar{\psi} \psi \rangle_{\text{sub}}$ is expected to behave well in the chiral limit, even though the contribution from the zero modes is divergent as a simple pole in the chiral limit. Hence, in the numerical study on the lattice, it is important to identify the would-be zero modes which correspond to the zero modes in the continuum limit, and to remove them in the calculation of the quark condensate.

Before proceeding, let us briefly go through the index theorem. In the continuum theory in Euclidean space, the axial Ward identity [17] is

$$\partial_\mu A_\mu(x) = 2mP(x) - 2N_f q(x). \quad (17)$$

Here $A_\mu \equiv \bar{\psi} \gamma_\mu \gamma_5 \psi$ is the axial vector current in the flavor singlet representation, $P \equiv \bar{\psi} \gamma_5 \psi$ is the corresponding pseudo-scalar operator, and $q \equiv \frac{1}{32\pi^2} \text{Tr}[F_{\mu\nu} \tilde{F}_{\mu\nu}]$ is the topological charge density (= winding number density). Now the topological charge Q is

$$Q \equiv \int d^4x \langle q(x) \rangle \quad (18)$$

$$= -\frac{1}{2N_f} \int d^4x \langle \partial_\mu A_\mu(x) - 2mP(x) \rangle \quad (19)$$

$$= \frac{m}{N_f} \int d^4x \langle \bar{\psi} \gamma_5 \psi \rangle \quad (20)$$

Using the spectral decomposition, we can rewrite Q as follows,

$$Q = -m \sum_\lambda \frac{1}{i\lambda + m} \int d^4x \left[u_\lambda^\dagger(x) \gamma_5 u_\lambda(x) \right]. \quad (21)$$

Noting that $\gamma_5 u_\lambda(x) = u_{-\lambda}(x)$ for $\lambda \neq 0$,

$$\int d^4x \left[u_\lambda^\dagger(x) \gamma_5 u_\lambda(x) \right] = \langle u_\lambda | u_{-\lambda} \rangle = 0. \quad (22)$$

Hence, only zero modes contribute to Q . For the zero modes, it is convenient to choose the helicity eigenstates as the basis vectors so that $\langle u_0^L | \gamma_5 | u_0^L \rangle = -1$ and $\langle u_0^R | \gamma_5 | u_0^R \rangle = +1$, where the superscripts L, R represent left-handed and right-handed helicity, respectively. Then deriving the index theorem is straightforward [1]:

$$Q = n_- - n_+, \quad (23)$$

where n_+ (n_-) is the number of the right-handed (left-handed) zero modes.

III. SPECTRAL DECOMPOSITION WITH STAGGERED FERMIONS

A number of improved versions of staggered fermions exist, such as HYP-smeared staggered fermions [5], asqtad improved staggered fermions [18], and highly improved staggered quarks (HISQ) [7]. Here we refer to all of them collectively as “staggered fermions.” Staggered fermions have four tastes per flavor by construction [19]. Hence, the quark condensate for staggered fermions is defined as

$$\langle \bar{\chi} \chi \rangle = -\frac{1}{VN_t} \left\langle \text{Tr} \left(\frac{1}{D_s + m} \right) \right\rangle_U, \quad (24)$$

where χ represents a staggered quark field, D_s is the staggered Dirac operator for a single valence flavor, V is the lattice volume, and N_t is the number of tastes. We measure the quark condensate using a stochastic method.

$$(D_s + m)_{x,y} \chi(y) = \xi(x) \quad (25)$$

$$\chi(x) = \left[\frac{1}{D_s + m} \right]_{x,y} \xi(y) \quad (26)$$

$$\text{Tr} \left(\frac{1}{D_s + m} \right) = \lim_{N_\xi \rightarrow \infty} \frac{1}{N_\xi} \sum_\xi \sum_y \xi^\dagger(y) \chi(y), \quad (27)$$

where x, y are representative indices which represent the space-time coordinates, taste, and color indices collectively. Here $\xi(x)$ represents either Gaussian random numbers or $U(1)$ noise random numbers which satisfy a simple identity:

$$\lim_{N_\xi \rightarrow \infty} \frac{1}{N_\xi} \sum_\xi \xi^\dagger(x) \xi(y) = \delta_{xy},$$

where N_ξ is the number of random vector samples.

Staggered fermions have a taste symmetry $SU(4)_L \otimes SU(4)_R \otimes U(1)_V$ in the continuum limit at $a = 0$ [20]. However, this symmetry breaks down to a subgroup $U(1)_V \otimes U(1)_A$ on the lattice with $a \neq 0$ [19, 20]. The remaining axial symmetry $U(1)_A$ plays an important role in protecting the quark mass from receiving an additive renormalization. In addition, it does not have any axial anomaly.

The Dirac operator (D_s) of staggered fermions is anti-Hermitian: $D_s^\dagger = -D_s$. Hence, its eigenvalues are purely imaginary:

$$D_s |f_\lambda^s\rangle = i\lambda |f_\lambda^s\rangle, \quad (28)$$

where λ is real. Here, the subscript s and superscript s represent staggered quarks.

In practice, when we obtain eigenvalues of D_s numerically, we use the following relationship instead of Eq. (28):

$$D_s^\dagger D_s |g_{\lambda^2}^s\rangle = \lambda^2 |g_{\lambda^2}^s\rangle \quad (29)$$

where the $|g_{\lambda^2}^s\rangle$ state is a mixture of the two eigenvectors $|f_{+\lambda}^s\rangle$ and $|f_{-\lambda}^s\rangle$. In other words,

$$|g_{\lambda^2}^s\rangle = c_1|f_{+\lambda}^s\rangle + c_2|f_{-\lambda}^s\rangle \quad (30)$$

where the c_i are complex numbers that satisfy the normalization condition

$$|c_1|^2 + |c_2|^2 = 1. \quad (31)$$

The numerical algorithm is a variation of a Lanczos algorithm adapted for lattice QCD [21]. Details on the numerical algorithms as well as comprehensive references are given in Appendix A.

Why do we obtain λ^2 instead of $i\lambda$? The first reason is that doing so allows us to use even-odd preconditioning [22], which makes Lanczos run on only even or odd sites on the lattice. This leads to two benefits: One is that there is a substantial gain in the speed of the code, and the other is that the code uses only half the memory otherwise required. Details on even-odd preconditioning are described in Appendix B. The second reason is that obtaining λ^2 instead of $i\lambda$ allows us to implement polynomial acceleration algorithms [23] into Lanczos more easily, since the eigenvalues of $D_s^\dagger D_s$ are positive definite and have a lower bound $\lambda^2 > 0$. Note that staggered fermions have would-be zero modes whose eigenvalues are small and positive ($\lambda^2 > 0$) on rough gauge configurations. There are no exact zero modes ($\lambda = 0$) with staggered fermions on rough gauge configurations [24]. Details of our implementation of polynomial acceleration are described in Appendix A.

Hence, we use the Lanczos algorithm to solve Eq. (29) for the eigenvector $|g_{\lambda^2}^s\rangle$ as well as the corresponding eigenvalue λ^2 . We obtain $|f_{+\lambda}^s\rangle$ and $|f_{-\lambda}^s\rangle$ by using projection operators defined as

$$P_+ = (D_s + i\lambda) \quad (32)$$

$$P_- = (D_s - i\lambda), \quad (33)$$

where P_+ is the projection operator that selects only the $|f_{+\lambda}^s\rangle$ component and removes the $|f_{-\lambda}^s\rangle$ component. Then

$$|\chi_+\rangle = P_+|g_{\lambda^2}^s\rangle \quad (34)$$

$$|\chi_-\rangle = P_-|g_{\lambda^2}^s\rangle \quad (35)$$

and the orthonormal eigenvectors are

$$|f_{+\lambda}^s\rangle = \frac{|\chi_+\rangle}{\sqrt{\langle\chi_+|\chi_+\rangle}} \quad (36)$$

$$|f_{-\lambda}^s\rangle = \frac{|\chi_-\rangle}{\sqrt{\langle\chi_-|\chi_-\rangle}}. \quad (37)$$

IV. CHIRAL SYMMETRY OF STAGGERED FERMIONS

The two vectors $|f_{\pm\lambda}^s\rangle$ are related to each other through a chiral Ward identity of staggered fermions. Here we

address this issue of the chiral symmetry of staggered fermions and its consequences. Let us begin with notation and definitions. We define staggered bilinear operators as

$$\begin{aligned} \mathcal{O}_{S \times T}(x) &\equiv \bar{\chi}(x_A)[\gamma_S \otimes \xi_T]_{AB}\chi(x_B) \\ &= \bar{\chi}_a(x_A)\overline{(\gamma_S \otimes \xi_T)}_{AB}U(x_A, x_B)_{ab}\chi_b(x_B) \end{aligned} \quad (38)$$

where χ_b are staggered quark fields, and a, b are color indices. Here the coordinate $x_A = 2x + A$ and A, B are hypercubic vectors with $A_\mu, B_\mu \in \{0, 1\}$, and

$$\overline{(\gamma_S \otimes \xi_T)}_{AB} \equiv \frac{1}{4}\text{Tr}(\gamma_A^\dagger \gamma_S \gamma_B \gamma_T^\dagger) \quad (39)$$

where γ_S represents the Dirac spin matrix, and ξ_T represents the 4×4 taste matrix. In addition,

$$\begin{aligned} U(x_A, x_B) &\equiv \mathbb{P}_{SU(3)} \left[\sum_{p \in \mathcal{C}} V(x_A, x_{p_1}) V(x_{p_1}, x_{p_2}) \right. \\ &\quad \left. \cdots V(x_{p_n}, x_B) \right] \end{aligned} \quad (40)$$

where $\mathbb{P}_{SU(3)}$ represents the $SU(3)$ projection, and \mathcal{C} represents the complete set of shortest paths from x_A to x_B . $V(x, y)$ represents the HYP-smeared fat link [5, 6] for HYP staggered fermions, the Fat7 fat link [6, 25–27] for asqtad staggered fermions or HISQ, and the thin gauge link for unimproved staggered fermions.

The conserved $U(1)_A$ axial symmetry transformation is

$$\begin{aligned} \Gamma_\epsilon(A, B, a, b) &\equiv [\gamma_5 \otimes \xi_5]_{AB;ab} \\ &= \overline{(\gamma_5 \otimes \xi_5)}_{AB} \cdot \delta_{ab} \\ &= \epsilon(A) \cdot \delta_{AB} \cdot \delta_{ab} \end{aligned} \quad (41)$$

where Γ_ϵ is often called “distance parity,” and

$$\epsilon(A) \equiv (-1)^{S_A} \quad (42)$$

$$S_A \equiv \sum_{\mu=1}^4 A_\mu. \quad (43)$$

Under the $U(1)_A$ transformation, the staggered Dirac operator transforms as follows,

$$\Gamma_\epsilon D_s \Gamma_\epsilon = D_s^\dagger = -D_s \quad (44)$$

$$\Gamma_\epsilon D_s = -D_s \Gamma_\epsilon. \quad (45)$$

Therefore,

$$\begin{aligned} D_s |f_{+\lambda}^s\rangle &= +i\lambda |f_{+\lambda}^s\rangle \\ D_s \Gamma_\epsilon |f_{+\lambda}^s\rangle &= -i\lambda \Gamma_\epsilon |f_{+\lambda}^s\rangle, \end{aligned} \quad (46)$$

and $f_{-\lambda}^s$ can be obtained from $f_{+\lambda}^s$ through Γ_ϵ transformation as follows,

$$\Gamma_\epsilon |f_{+\lambda}^s\rangle = e^{+i\theta} |f_{-\lambda}^s\rangle$$

$$\Gamma_\epsilon |f_{-\lambda}^s\rangle = e^{-i\theta} |f_{+\lambda}^s\rangle. \quad (47)$$

In general, there is no constraint for the real phase θ , so we expect its probability distribution to be random. In practice, however, we make use of even-odd preconditioning, and we obtain the odd site fermion fields ($|g_o\rangle$) from the even site fermion fields ($|g_e\rangle$) with the relation $|g_o\rangle = \eta D_{oe} |g_e\rangle$, where D_{oe} is a sector of D_s that connects even site fields to odd site fields, and η is a random complex number. Hence the distribution of θ depends on our choice of η . In our numerical study, we set $\eta = 1$. Then θ is given by

$$\theta = \pi + 2\beta, \quad \beta = \arctan(\lambda). \quad (48)$$

Details on the even-odd preconditioning and the derivation of Eq. (48) are explained in Appendix B.

We expect that if there exists an eigenvector $|f_{+\lambda}^s\rangle$, there must be a corresponding parity partner $|f_{-\lambda}^s\rangle$ due to the exact chiral symmetry Γ_ϵ . In other words, the Ward identity of Eq. (47) comes directly from the conserved $U(1)_A$ axial symmetry.

A. Numerical Examples

We now use numerical examples to demonstrate how the above theory works in quenched QCD. In Table I, details of the gauge configurations are presented.

TABLE I. Input parameters for numerical study in quenched QCD. For more details, refer to Ref. [9]. The relationship between sample sizes in our study and the number of the gauge configurations is non-trivial and discussed later.

parameters	values
gluon action	tree level Symanzik [28–30]
tadpole improvement	yes
β	5.0
geometry	20^4
a	0.077(1) fm [31]
$1/a$	2.6 GeV
valence quarks	HYP staggered fermions [6, 32, 33]
N_f	$N_f = 0$ (quenched QCD)

We measure the topological charge Q using gauge links. We use the $Q(5\text{Li})$ operator defined in Ref. [34, 35] after 10 \sim 30 iterations of APE smearing with $\alpha = 0.45$ [36–38]. We show an example of the eigenvalue spectrum for $Q = 0$ in Fig. 1. Since $Q = 0$, we do not expect to find any zero modes for this gauge configuration. In Fig. 1(a), we show eigenvalues λ^2 for the eigenvectors $|g_{\lambda^2}^s\rangle$ defined in Eq. (29). Here we observe eight-fold degeneracy for non-zero eigenmodes due to the conserved $U(1)_A$ axial symmetry. Here $\lambda_2 = -\lambda_1$ and, in general, $\lambda_{2n} = -\lambda_{2n-1}$ for integer $n > 0$. In other words, λ_{2n} is the parity partner of λ_{2n-1} . For each λ_i , there

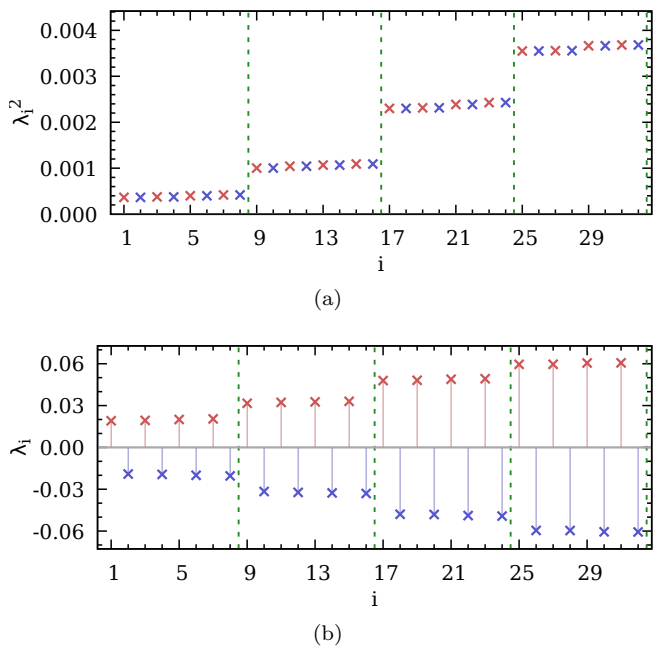


FIG. 1. Eigenvalue spectrum of staggered Dirac operator on a $Q = 0$ gauge configuration.

exists four-fold degeneracy due to approximate $SU(4)$ taste symmetry. For each of these four-fold degenerate eigenvalues (for example $\lambda_1, \lambda_3, \lambda_5, \lambda_7$ in Fig. 1(a)), there exists a parity partner eigenvalue due to the $U(1)_A$ symmetry: $\lambda_2 = -\lambda_1$, $\lambda_4 = -\lambda_3$, $\lambda_6 = -\lambda_5$, and $\lambda_8 = -\lambda_7$ (refer to Fig. 1(b)).

Let us turn to an example with $Q = -1$. Since $Q = -1$, we expect to observe four-fold degenerate zero modes. The gauge configurations are so rough that we expect to observe not exact zero modes but would-be zero modes. In Fig. 2, we demonstrate how the would-be zero modes behave on a gauge configuration with $Q = -1$. As one can see in Figs. 2(a) and 2(b), we find four-fold degenerate would-be zero modes: $\lambda_1, \lambda_2, \lambda_3, \lambda_4$. Thanks to the $U(1)_A$ chiral Ward identity in Eq. (47), we find that $\lambda_2 = -\lambda_1$ and $\lambda_4 = -\lambda_3$. As in the case with $Q = 0$, we find that the non-zero eigenmodes are eight-fold degenerate. This pattern of four-fold degeneracy for would-be zero modes and eight-fold degeneracy for non-zero modes is also observed in the cases with $Q = -2$ and $Q = -3$, which are presented in Appendix C.

At this point, the reader may have already concluded that we can distinguish would-be zero modes of staggered quarks from non-zero modes by counting the degeneracy of the eigenvalues [8, 9, 39]. This conclusion is true but can lead to wrong answers in practice. The reason is that, on large lattices, the eigenvalues are so dense that visually distinguishing between 4-fold and 8-fold degeneracies is typically impossible. Hence, we need a practical and robust method to identify would-be zero modes and non-zero modes of staggered fermions. The introduction of such a method is the main subject of the next section,

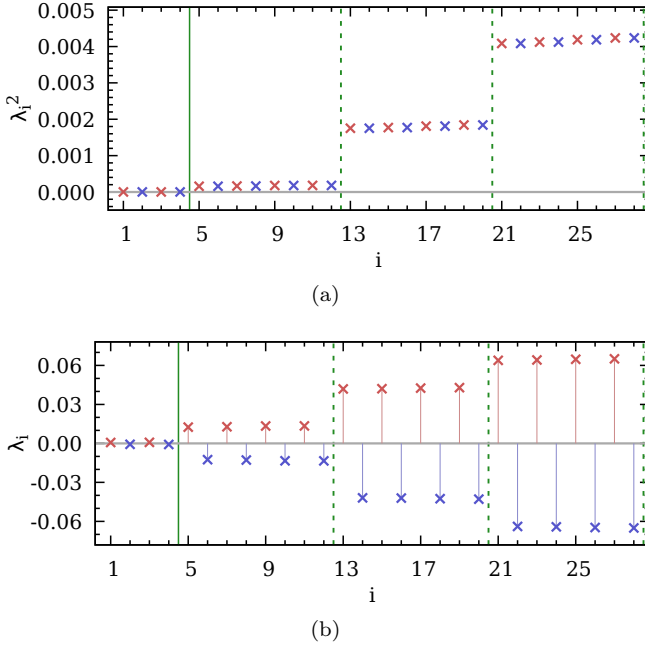


FIG. 2. Eigenvalue spectrum of staggered Dirac operator on a $Q = -1$ gauge configuration.

Sec. V.

Using the chiral Ward identity of Eq. (47), we can measure the phase θ numerically. In Fig. 3, we show numerical results (red circles) for θ . Here, the blue line represents the theoretical prediction given in Eq. (48). We find the results are consistent with the prediction within numerical precision.

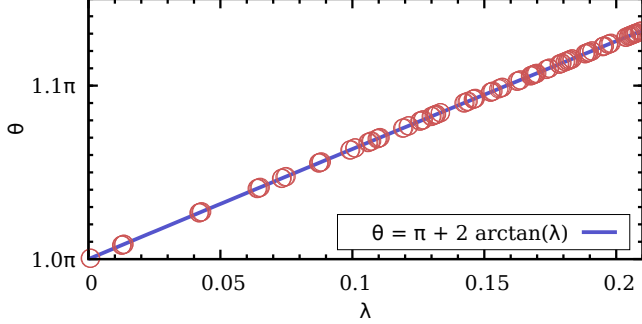


FIG. 3. The phase θ as a function of λ . Red circles represent numerical results for θ . The blue line represents the prediction from the theory. Here we use a gauge configuration with $Q = -1$ for the measurement.

V. CHIRALITY MEASUREMENT

To simplify the notation, we introduce the following convention for eigenvalue indices,

$$D_s|f_j\rangle = i\lambda_j|f_j\rangle, \quad (49)$$

where $|f_j\rangle = |f_{\lambda_j}^s\rangle$ is defined in Eq. (28). We define the chirality operator and abbreviations as follows.

$$\begin{aligned} \Gamma_5(\lambda_i, \lambda_j) &\equiv \langle f_i | [\gamma_5 \otimes 1] | f_j \rangle \\ &\equiv \int d^4x [f_{\lambda_i}^s(x_A)]^\dagger [\gamma_5 \otimes 1]_{x;AB} f_{\lambda_j}^s(x_B), \end{aligned} \quad (50)$$

$$(\Gamma_5)_j^i \equiv \Gamma_5(\lambda_i, \lambda_j), \quad (51)$$

$$|\Gamma_5|_j^i \equiv |\Gamma_5(\lambda_i, \lambda_j)|, \quad (52)$$

where x_A and $[\gamma_5 \otimes 1]$ are defined in Eqs. (38)-(40), and λ_i and λ_j represent eigenvalues of D_s . The chirality operator $[\gamma_5 \otimes 1]$ satisfies the same relationships as the continuum chirality operator γ_5 .

$$[\gamma_5 \otimes 1]^{2n+1} = [\gamma_5 \otimes 1], \quad (53)$$

$$[\gamma_5 \otimes 1]^{2n} = [1 \otimes 1], \quad (54)$$

$$\left[\frac{1}{2}(1 \pm \gamma_5) \otimes 1\right]^n = \left[\frac{1}{2}(1 \pm \gamma_5) \otimes 1\right], \quad (55)$$

$$\left[\frac{1}{2}(1 + \gamma_5) \otimes 1\right] \left[\frac{1}{2}(1 - \gamma_5) \otimes 1\right] = 0, \quad (56)$$

where n is a non-negative integer. A rigorous proof of Eqs. (53)-(56) is given in Appendix D.

Our definition of the chirality operator $[\gamma_5 \otimes 1]$ is different from that used in Refs. [8, 13, 24]. The old chirality operator of Refs. [8, 13, 24] does not satisfy the recursion relations of Eqs. (53)-(56). In addition, it does not satisfy the chiral Ward identities of Eqs. (62)-(64). This difference is addressed in Appendix D. The bottom line is that the conventional chirality operator does not satisfy the recursion relationships in Eqs. (53)-(56), even though it is classified according to the true irreducible representation (irrep) of the lattice rotational symmetry group [40-42].

For further discussion we define another operator $[1 \otimes \xi_5]$, which we call the “(maximal) shift operator,”

$$\begin{aligned} \Xi_5(\lambda_i, \lambda_j) &\equiv \langle f_i | [1 \otimes \xi_5] | f_j \rangle \\ &\equiv \int d^4x [f_{\lambda_i}^s(x_A)]^\dagger [1 \otimes \xi_5]_{x;AB} f_{\lambda_j}^s(x_B), \end{aligned} \quad (57)$$

$$(\Xi_5)_j^i \equiv \Xi_5(\lambda_i, \lambda_j), \quad (58)$$

$$|\Xi_5|_j^i \equiv |\Xi_5(\lambda_i, \lambda_j)|. \quad (59)$$

This shift operator satisfies the following recursion relations:

$$[1 \otimes \xi_5]^{2n+1} = [1 \otimes \xi_5], \quad (60)$$

$$[1 \otimes \xi_5]^{2n} = [1 \otimes 1], \quad (61)$$

where n is a non-negative integer. The conserved $U(1)_A$ symmetry transformation can be expressed in terms of the chirality operator and the shift operator as follows,

$$\Gamma_\epsilon \equiv [\gamma_5 \otimes \xi_5]$$

$$\begin{aligned}
&= [\gamma_5 \otimes 1][1 \otimes \xi_5] \\
&= [1 \otimes \xi_5][\gamma_5 \otimes 1].
\end{aligned} \tag{62}$$

In addition, the chirality and shift operators satisfy the following relations:

$$\Gamma_\epsilon[\gamma_5 \otimes 1] = [\gamma_5 \otimes 1]\Gamma_\epsilon = [1 \otimes \xi_5], \tag{63}$$

$$\Gamma_\epsilon[1 \otimes \xi_5] = [1 \otimes \xi_5]\Gamma_\epsilon = [\gamma_5 \otimes 1]. \tag{64}$$

Therefore, we obtain the Ward identities:

$$\begin{aligned}
e^{+i\theta}[\gamma_5 \otimes 1]|f_{-i}\rangle &= [1 \otimes \xi_5]|f_{+i}\rangle, \\
e^{-i\theta}[\gamma_5 \otimes 1]|f_{+i}\rangle &= [1 \otimes \xi_5]|f_{-i}\rangle,
\end{aligned} \tag{65}$$

where

$$|f_{\pm i}\rangle \equiv |f_{\pm\lambda_i}^s\rangle. \tag{66}$$

Hence, we define the spectral decomposition by

$$[\gamma_5 \otimes 1]|f_j\rangle = \sum_i (\Gamma_5)_j^i |f_i\rangle \tag{67}$$

where we use Eqs. (50) and (51). Similarly,

$$[1 \otimes \xi_5]|f_j\rangle = \sum_i (\Xi_5)_j^i |f_i\rangle \tag{68}$$

where we use Eqs. (57) and (58). Thanks to the Ward identities of Eq. (65), we obtain

$$\begin{aligned}
e^{-i\theta}\Gamma_5(\lambda_i, +\lambda_j) &= \Xi_5(\lambda_i, -\lambda_j) \\
e^{-i\theta}(\Gamma_5)_{+j}^i &= (\Xi_5)_{-j}^i \\
|\Gamma_5|_{+j}^i &= |\Xi_5|_{-j}^i.
\end{aligned} \tag{69}$$

Similarly,

$$\begin{aligned}
e^{+i\theta}\Gamma_5(\lambda_i, -\lambda_j) &= \Xi_5(\lambda_i, +\lambda_j) \\
e^{+i\theta}(\Gamma_5)_{-j}^i &= (\Xi_5)_{+j}^i \\
|\Gamma_5|_{-j}^i &= |\Xi_5|_{+j}^i.
\end{aligned} \tag{70}$$

Applying Γ_ϵ to both sides of Eq. (67), we obtain

$$[1 \otimes \xi_5]|f_j\rangle = \sum_\ell (\Gamma_5)_j^\ell e^{i\theta_\ell} |f_{-\ell}\rangle \tag{71}$$

$$= \sum_i (\Xi_5)_j^i |f_i\rangle. \tag{72}$$

Hence, we obtain another Ward identity:

$$|\Gamma_5|_j^{-i} = |\Xi_5|_j^{+i}. \tag{73}$$

Similarly, we can obtain the Ward identities:

$$|\Gamma_5|_{-j}^{-i} = |\Xi_5|_{-j}^{+i}, \tag{74}$$

$$|\Gamma_5|_j^{+i} = |\Xi_5|_j^{-i}. \tag{75}$$

We can summarize all the results of Eqs. (69)-(75) in the following form:

$$|\Gamma_5|_j^i = |\Xi_5|_j^{-i} = |\Xi_5|_{-j}^i = |\Gamma_5|_{-j}^{-i}, \tag{76}$$

$$\begin{aligned}
\Leftrightarrow |\Gamma_5(\lambda_i, \lambda_j)| &= |\Xi_5(-\lambda_i, \lambda_j)| = |\Xi_5(\lambda_i, -\lambda_j)| \\
&= |\Gamma_5(-\lambda_i, -\lambda_j)|.
\end{aligned} \tag{77}$$

In addition, Hermiticity ensures that we can interchange λ_i and λ_j , which gives the final form of the chiral Ward identities.

$$|\Gamma_5|_j^i = |\Xi_5|_j^{-i} = |\Xi_5|_{-j}^i = |\Gamma_5|_{-j}^{-i} = |\Gamma_5|_i^j = |\Xi_5|_i^{-j} = |\Xi_5|_{-i}^j = |\Gamma_5|_{-i}^{-j} \tag{78}$$

$$\begin{aligned}
\Leftrightarrow |\Gamma_5(\lambda_i, \lambda_j)| &= |\Xi_5(-\lambda_i, \lambda_j)| = |\Xi_5(\lambda_i, -\lambda_j)| = |\Gamma_5(-\lambda_i, -\lambda_j)| = |\Gamma_5(\lambda_j, \lambda_i)| = |\Xi_5(-\lambda_j, \lambda_i)| \\
&= |\Xi_5(\lambda_j, -\lambda_i)| = |\Gamma_5(-\lambda_j, -\lambda_i)|.
\end{aligned} \tag{79}$$

The quantity $(|\Gamma_5|_j^i)^2$ for $i \neq j$ represents the leakage probability of the chirality operator. We call $|\Gamma_5|_j^i$ the leakage parameter for the chirality operator. Similarly, the quantity $(|\Xi_5|_j^i)^2$ for $i \neq j$ represents the leakage probability of the shift operator, and we call $|\Xi_5|_j^i$ the leakage parameter for the shift operator. By examining the leakage pattern, we can distinguish zero modes and non-zero modes, which is the main subject of the next subsections.

A. Eigenvalue spectrum of D_s in the continuum

Here we consider staggered quark actions at $a = 0$. We define a general form of the shift operator corresponding to a generator of the $SU(4)$ taste symmetry:

$$\Xi_F = [1 \otimes \xi_F], \tag{80}$$

$$\xi_F \in \{ \xi_5, \xi_\mu, \xi_{\mu 5}, \xi_{\mu\nu} \} \quad \text{for } \mu \neq \nu, \tag{81}$$

where ξ_μ respects the Clifford algebra $\{\xi_\mu, \xi_\nu\} = 2\delta_{\mu\nu}$ in Euclidean space.

Let us consider the following quantity W_1 in the continuum:

$$W_1 \equiv \langle f_\ell | \Xi_F D_s | f_n \rangle \tag{82}$$

$$D_s|f_n\rangle = i\lambda_n|f_n\rangle. \quad (83)$$

Since the $SU(4)$ taste symmetry is exactly conserved in the continuum, we know that

$$[\Xi_F, D_s] = 0 \quad (84)$$

Hence, we find the following Ward identity:

$$W_1 = \langle f_\ell | \Xi_F D_s | f_n \rangle = i\lambda_n \langle f_\ell | \Xi_F | f_n \rangle \quad (85)$$

$$= \langle f_\ell | D_s \Xi_F | f_n \rangle = i\lambda_\ell \langle f_\ell | \Xi_F | f_n \rangle \quad (86)$$

and therefore

$$i(\lambda_\ell - \lambda_n) \cdot \langle f_\ell | \Xi_F | f_n \rangle = 0. \quad (87)$$

Hence, in the continuum, we find the following properties of the eigenvalue spectrum:

- If $\lambda_\ell \neq \lambda_n$, $(\Xi_F)_n^\ell = \langle f_\ell | \Xi_F | f_n \rangle = 0$. In other words, if the eigenvalues are different, there is no leakage ($(\Xi_F)_n^\ell = 0$) between the two eigenmodes.
- If $\lambda_j \equiv \lambda_\ell = \lambda_n$, $(\Xi_F)_n^\ell \neq 0$ is possible. In this case, the eigenvalues are degenerate and belong to a quartet such that

$$D_s|f_{j,m}\rangle = i\lambda_j|f_{j,m}\rangle \quad (88)$$

$$|f_\ell\rangle, |f_n\rangle \in \{|f_{j,m}\rangle \text{ with } m = 1, 2, 3, 4\}, \quad (89)$$

where m is a taste index which represents the four-fold degeneracy for the eigenvalue λ_j , $|f_\ell\rangle$ and $|f_n\rangle$ are linear combinations of the quartet $\{|f_{j,m}\rangle\}$, and the eigenvectors for different m are orthogonal to each other by construction due to the Lanczos algorithm.

- We know that the staggered fermion field $\chi^c(x_A)$ is mapped into the continuum fermion field $\psi_{\alpha;t}^c(x)$, where α represents a Dirac spinor index, c represents a color index, and $t = 1, 2, 3, 4$ represents a taste index. Hence, for a given eigenvalue λ_j , there remain four degrees of freedom which come from the taste index. Accordingly, for a given eigenvalue λ_j , there are four degenerate eigenstates $|f_{j,m}\rangle$ with $m = 1, 2, 3, 4$.
- If we know all four eigenstates $\{|f_{j,m}\rangle\}$ for a certain eigenvalue λ_j , we find that

$$\begin{aligned} \text{Tr}(\Xi_F) &= \sum_{m=1}^4 (\Xi_F)_{j,m}^{j,m} \\ &= \sum_{m=1}^4 \langle f_{j,m} | \Xi_F | f_{j,m} \rangle = 0 \end{aligned} \quad (90)$$

This is because the $SU(4)$ group generators are traceless in the fundamental representation.

However, on the lattice at $a \neq 0$, the taste symmetry is broken by terms of order $a^2\alpha_s^n$ with $n \geq 1$, which is explained in Ref. [20]. In addition, for $a \neq 0$,

$$D_s|f_{j,m}\rangle = i\lambda_{j,m}|f_{j,m}\rangle \quad (91)$$

and $\lambda_{j,m} \neq \lambda_{j,m'}$ in general for $m \neq m'$, which reflects the taste symmetry breaking effect at $a \neq 0$. We know that $\lambda_{j,m} = \lambda_{j,m'}$ for all m, m' in the continuum ($a = 0$) due to the exact taste symmetry. Hence, on the finite lattice, we expect a small deviation from the above continuum properties. A good barometer to measure this effect is to monitor T_5

$$T_5 \equiv \frac{1}{4} \text{Tr}(\Xi_5) = \frac{1}{4} \sum_m (\Xi_5)_{j,m}^{j,m} \quad (92)$$

and measure how much it deviates from zero (the continuum value). Another direct barometer to measure effects of taste symmetry breaking is the leakage S_5 from one quartet (λ_ℓ) to another quartet (λ_j) with $\lambda_\ell \neq \lambda_j$.

$$S_5 \equiv \frac{1}{16} \sum_{m,m'} |\Xi_5|_{j,m'}^{\ell,m} = \frac{1}{16} \sum_{m,m'} |\langle f_{\ell,m} | \Xi_5 | f_{j,m'} \rangle| \quad (93)$$

The size of the leakage S_5 indicates directly how much the taste symmetry is broken at $a \neq 0$, since $S_5 = 0$ in the continuum. We present numerical results for T_5 and S_5 in the next subsection.

B. Numerical study on chirality and leakage

Here we use dual notations for the eigenmodes: One is the serial index i for λ_i and the other is the quartet index j with taste index m for $\lambda_{j,m}$. The serial index is convenient for the plots, tables, and leakage patterns such as $|\Gamma_5|_b^a$, while the quartet index is convenient to explain the eigenstates classified by the taste symmetry group. The one-to-one mapping from the serial index i to the quartet indices j, m is given in Table II for the quartet index $j = 0, \pm 1$ when $Q = \pm 1$. The mapping for the quartet index $j = \pm 2$ (non-zero modes) is similar.

In Fig. 4, we present the leakage pattern of the zero mode of λ_1 and its parity partner $\lambda_2 = -\lambda_1$. Since $Q = -1$ in Fig. 4, we expect to observe four-fold degenerate would-be zero modes within a single quartet (quartet index $j = 0$).

$$\lim_{a \rightarrow 0} \lambda_i = 0 \quad \text{for } i = 1, 2, 3, 4. \quad (94)$$

In the continuum limit ($a = 0$), the $SU(4)$ taste symmetry becomes exactly conserved and so would-be zero modes become exact zero modes. However, at finite lattice spacing $a \neq 0$, the gauge configuration is sufficiently rough that would-be zero modes have non-zero eigenvalues: $\lambda_2 = -\lambda_1$, $\lambda_4 = -\lambda_3$, and $\lambda_1 \neq \lambda_3$ for $\lambda_1, \lambda_3 > 0$.

In Fig. 4(a), we show the leakage pattern of $|\Gamma_5|_1^i = |\Gamma_5(\lambda_i, \lambda_1)| = |\langle f_i | \Gamma_5 | f_1 \rangle|$. We find that there is, in practice, no leakage, and so the only non-zero component is

TABLE II. One-to-one mapping of serial index i of the λ_i eigenstate into a quartet index j and taste index m for $\lambda_{j,m} = \lambda_i$. Here $\lambda_{2n} = -\lambda_{2n-1}$ and $\lambda_{-j,m} = -\lambda_{+j,m}$. Here we assume $Q = \pm 1$.

λ_i	$\lambda_{j,m}$	i	j	m	mode
λ_1	$\lambda_{0,1}$	1	0	1	zero
λ_2	$\lambda_{0,2}$	2	0	2	zero
λ_3	$\lambda_{0,3}$	3	0	3	zero
λ_4	$\lambda_{0,4}$	4	0	4	zero
λ_5	$\lambda_{+1,1}$	5	+1	1	non-zero
λ_7	$\lambda_{+1,2}$	7	+1	2	non-zero
λ_9	$\lambda_{+1,3}$	9	+1	3	non-zero
λ_{11}	$\lambda_{+1,4}$	11	+1	4	non-zero
λ_6	$\lambda_{-1,1}$	6	-1	1	non-zero
λ_8	$\lambda_{-1,2}$	8	-1	2	non-zero
λ_{10}	$\lambda_{-1,3}$	10	-1	3	non-zero
λ_{12}	$\lambda_{-1,4}$	12	-1	4	non-zero

TABLE III. Numerical values for leakage patterns from the λ_1 eigenstate to the λ_i eigenstate in Fig. 4. Here, j represents a quartet index for the λ_i eigenstate. The leakage represents $|\mathcal{O}|_1^i = |\mathcal{O}(\lambda_i, \lambda_1)| = |\langle f_i | \mathcal{O} | f_1 \rangle|$ for $\mathcal{O} = \Gamma_5, \Xi_5$.

j	leakage	value	Ward id.
0	$ \Gamma_5 _1^1$	0.82382566818582	$= \Xi_5 _1^2$
0	$ \Xi_5 _1^2$	0.82382566818581	$= \Xi_5 _1^2$
0	$ \Xi_5 _2^1$	0.82382566818580	$= \Gamma_5 _2^2$
0	$ \Gamma_5 _2^2$	0.82382566818579	$= \Gamma_5 _1^1$
0	$ \Gamma_5 _1^2$	6.67×10^{-4}	
0	$ \Gamma_5 _1^3$	1.34×10^{-3}	
0	$ \Gamma_5 _1^4$	1.79×10^{-3}	
+1	$ \Gamma_5 _1^5$	2.56×10^{-2}	
-1	$ \Gamma_5 _1^6$	2.54×10^{-2}	
+2	$ \Gamma_5 _1^{13}$	5.77×10^{-3}	
-2	$ \Gamma_5 _1^{14}$	1.18×10^{-2}	

$|\Gamma_5|_1^1 = |\Gamma_5(\lambda_1, \lambda_1)|$. The other components are practically zero. In Figs. 4 (b), 4 (c), and 4 (d), we find that the Ward identity of Eqs. (78) and (79) is well-respected by the numerical results. In other words, the Ward identity $|\Gamma_5|_1^1 = |\Xi_5|_1^2 = |\Xi_5|_2^1 = |\Gamma_5|_2^2$ is satisfied within the numerical precision of the computer. Please refer to Table III for numerical details. This confirms that the theoretical prediction from the Ward identity in Eqs. (78) and (79) is correct.

In Fig. 4 (a), we find that there is small leakage into other quartets ($j = \pm 1, \pm 2$). The typical size of leakage between off-diagonal elements of the would-be zero modes, the $j = 0$ quartet, (e.g. $|\Gamma_5|_1^3$) is of order 10^{-3} . We also observe small leakage patterns of order $10^{-2} \sim 10^{-3}$ from the would-be zero modes, the $j = 0$ quartet, to the non-zero modes, the $j = \pm 1, \pm 2$ quartets (e.g. $|\Gamma_5|_1^5$).

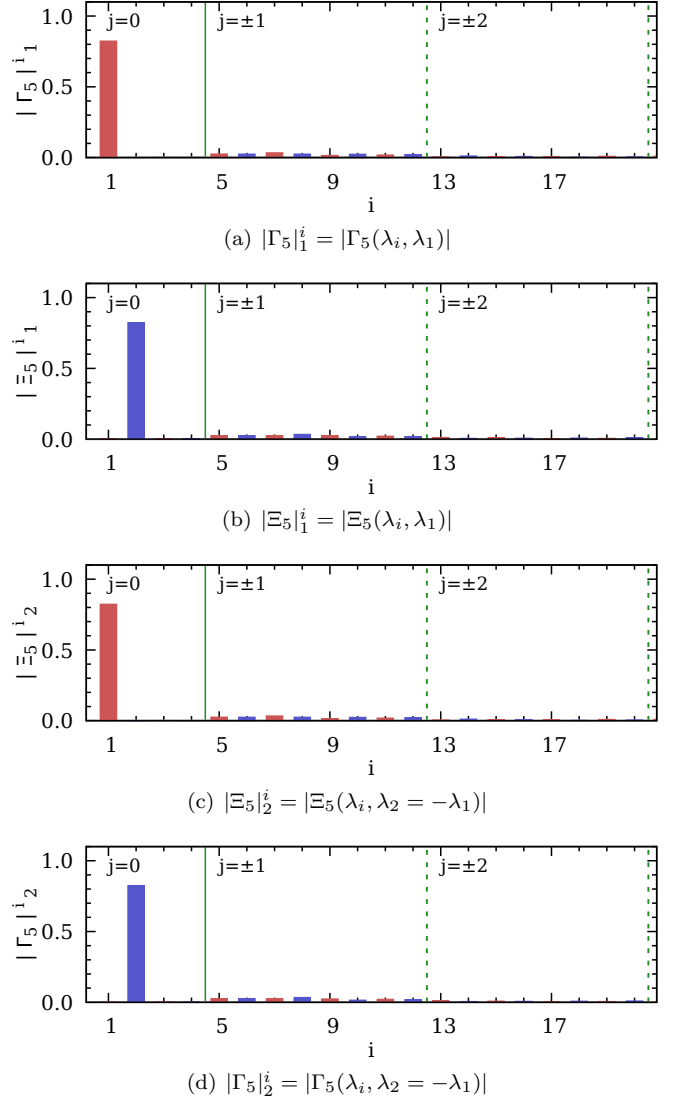
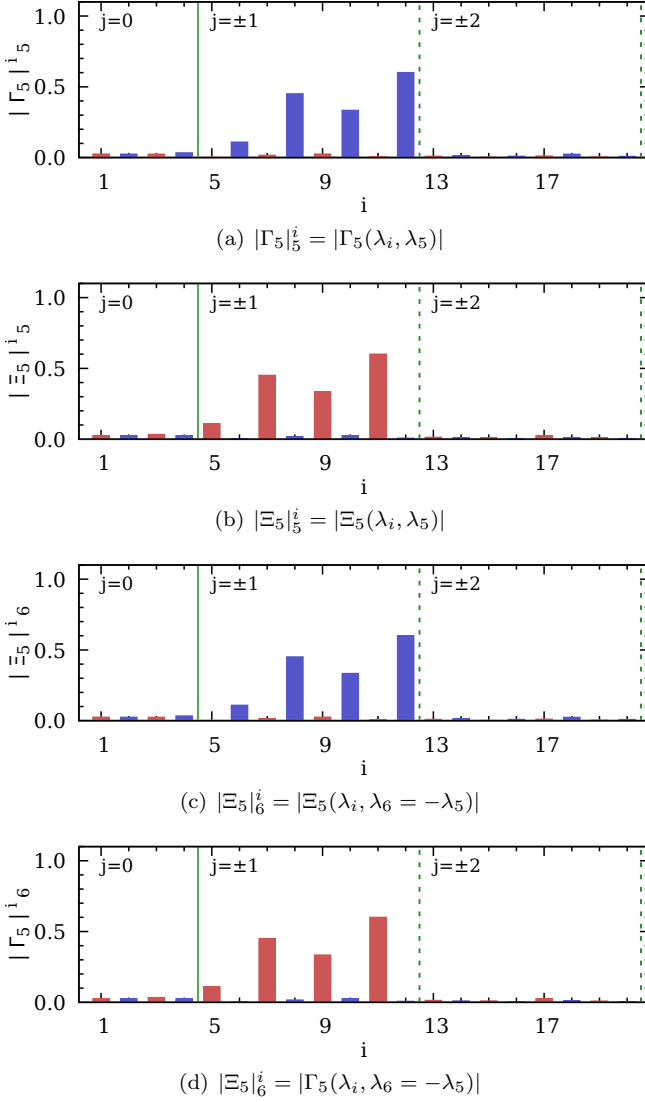


FIG. 4. Leakage pattern for would-be zero modes at $Q = -1$. Here, the red bar represents leakage to $\lambda_{i=2n-1} > 0$ with i odd, and the blue bar represents leakage to its parity partner $\lambda_{i=2n} = -\lambda_{2n-1}$ with i even.

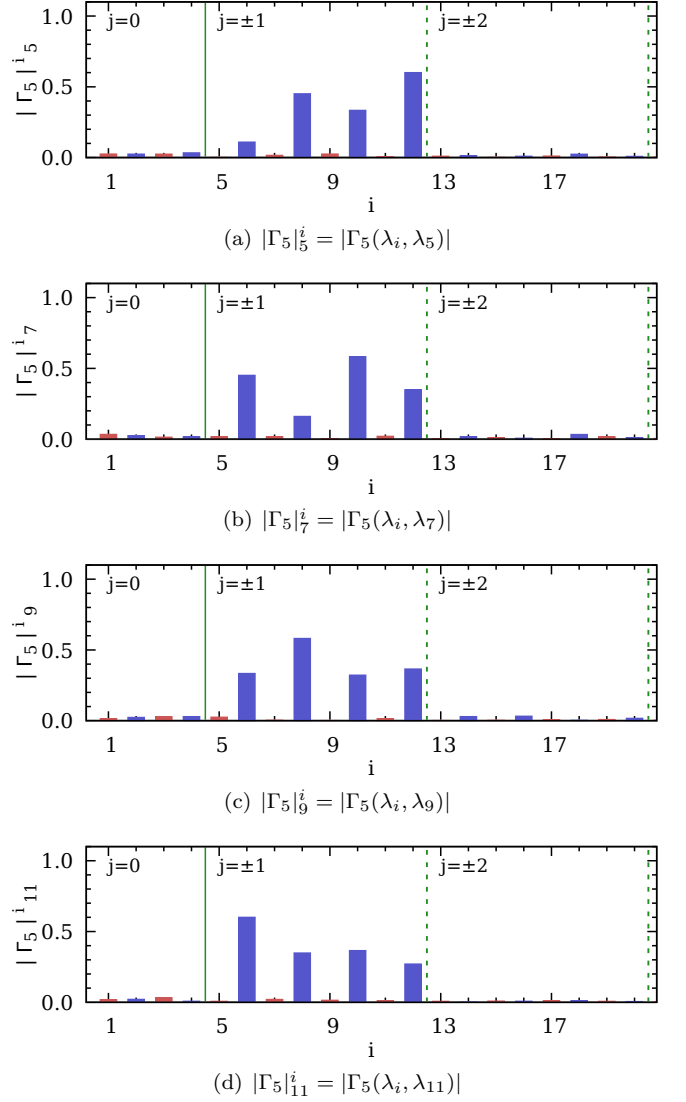
Now let us consider non-zero modes in the $j = +1$ quartet. In Fig. 5, we present the leakage pattern for the non-zero modes of λ_5 and its parity partner $\lambda_6 = -\lambda_5$. Even in the continuum limit ($a = 0$), $\lambda_5 \neq 0$, and so it is a non-zero mode. Thanks to the approximate $SU(4)$ taste symmetry and the exact $U(1)_A$ axial symmetry, there will be eight-fold degeneracy in the family of eight eigenstates composed of the $j = +1$ quartet, to which λ_5 belongs, and the $j = -1$ quartet (the parity partners). These eight-fold degenerate modes are designated together as $j = \pm 1$ quartets in Fig. 5, where they are a set of $\{\lambda_i\}$ with $5 \leq i \leq 12$.

Let us scrutinize the leakage pattern of the non-zero mode $\lambda_5 = \lambda_{j=+1, m=1}$. In Fig. 5 (a), first note that there is practically no leakage in the Γ_5 chirality mea-

FIG. 5. Leakage pattern for non-zero modes at $Q = -1$.

surement from λ_5 into λ_{2n-1} with $n > 0$. In other words, $|\Gamma_5|_5^{2n-1} = |\Gamma_5(\lambda_{2n-1}, \lambda_5)| \cong 0$. This implies that the chirality operator on the non-zero mode with $\lambda > 0$ leaks into only the parity partner modes with $\lambda < 0$. Second, note that the nontrivial leakage goes to those eigenstates in the $j = -1$ quartet such as $\{\lambda_6, \lambda_8, \lambda_{10}, \lambda_{12}\} = \{\lambda_{j,m} | j = -1, m = 1, 2, 3, 4\}$. In addition, we find that the Ward identity of Eqs. (78) and (79) is well-respected within the numerical precision in Figs. 5 (a), 5 (b), 5 (c), and 5 (d). In Table IV, we present numerical values of the $|\Gamma_5|_5^i$ shown in Fig. 5 (a).

Let us examine the $\Gamma_5 = [\gamma_5 \otimes 1]$ leakage pattern of the $j = +1$ quartet of the non-zero modes $\{\lambda_5, \lambda_7, \lambda_9, \lambda_{11}\}$. In Fig. 6, we find that the chirality measurement vanishes; $(\Gamma_5)_i^i = \Gamma_5(\lambda_i, \lambda_i) = 0$ for λ_i in the $j = +1$ quartet of non-zero modes. We also find that the Γ_5 leakage of $\lambda_{+1,m} > 0$ of the $j = +1$ quartet goes to the parity partners with $\lambda_{-1,m'} < 0$ of the $j = -1$ quartet, and the

FIG. 6. $[\gamma_5 \otimes 1]$ leakage pattern for non-zero modes at $Q = -1$.

leakage to other quartets such as $j = \pm 2$ is negligibly small compared to the leakage to the $j = -1$ quartet. The numerical values of $|\Gamma_5|_{+1,m'}^{-1,m}$ are summarized in Table V.

Let us examine the $\Xi_5 = [1 \otimes \xi_5]$ leakage pattern of the $j = +1$ quartet of the non-zero modes $\{\lambda_5, \lambda_7, \lambda_9, \lambda_{11}\}$. In Fig. 7, we find that the Ξ_5 leakage from the $j = +1$ quartet to the $j = -1$ quartet (parity partners) vanishes in practice. Since the leakage pattern of Ξ_5 is related to the leakage pattern of Γ_5 by the Ward identity

$$|\Xi_5|_{j',m'}^{j,m} = |\Gamma_5|_{j',m'}^{-j,m}, \quad (95)$$

Fig. 7 can be obtained from Fig. 6 using the Ward identity. We find that the Ξ_5 leakage from the $j = +1$ quartet to other quartets such as $j = \pm 2$ quartets is negligibly small compared to leakage to itself (the $j = +1$ quartet). Leakage patterns of the Γ_5 chirality and Ξ_5 shift operators for diverse topological charges are shown in

TABLE IV. Numerical values for data in Fig. 5.

j	leakage	value	Ward identities
-1	$ \Gamma_5 _5^6$	0.110	$= \Xi_5 _5^5 = \Xi_5 _6^6 = \Gamma_5 _6^5$
-1	$ \Gamma_5 _5^8$	0.452	$= \Xi_5 _5^7 = \Xi_5 _6^8 = \Gamma_5 _6^7 = \Gamma_5 _8^5 = \Xi_5 _7^5 = \Xi_5 _8^6 = \Gamma_5 _7^6$
-1	$ \Gamma_5 _5^{10}$	0.334	$= \Xi_5 _5^9 = \Xi_5 _6^{10} = \Gamma_5 _6^9 = \Gamma_5 _{10}^5 = \Xi_5 _9^5 = \Xi_5 _{10}^6 = \Gamma_5 _9^6$
-1	$ \Gamma_5 _5^{12}$	0.601	$= \Xi_5 _5^{11} = \Xi_5 _6^{12} = \Gamma_5 _6^{11} = \Gamma_5 _{12}^5 = \Xi_5 _{11}^5 = \Xi_5 _{12}^6 = \Gamma_5 _{11}^6$
+1	$ \Gamma_5 _5^5$	2.05×10^{-3}	$= \Xi_5 _6^6 = \Xi_5 _5^5 = \Gamma_5 _6^6$
+1	$ \Gamma_5 _5^7$	16.7×10^{-3}	$= \Xi_5 _5^8 = \Xi_5 _6^7 = \Gamma_5 _6^8 = \Gamma_5 _7^5 = \Xi_5 _8^5 = \Xi_5 _7^6 = \Gamma_5 _8^6$
+1	$ \Gamma_5 _5^9$	25.6×10^{-3}	$= \Xi_5 _5^{10} = \Xi_5 _6^9 = \Gamma_5 _6^{10} = \Gamma_5 _9^5 = \Xi_5 _{10}^5 = \Xi_5 _9^6 = \Gamma_5 _{10}^6$
+1	$ \Gamma_5 _5^{11}$	7.32×10^{-3}	$= \Xi_5 _5^{12} = \Xi_5 _6^{11} = \Gamma_5 _6^{12} = \Gamma_5 _{11}^5 = \Xi_5 _{12}^5 = \Xi_5 _{11}^6 = \Gamma_5 _{12}^6$
0	$ \Gamma_5 _5^3$	2.52×10^{-2}	
0	$ \Gamma_5 _5^4$	3.43×10^{-2}	
+2	$ \Gamma_5 _5^{13}$	1.02×10^{-2}	
-2	$ \Gamma_5 _5^{14}$	1.38×10^{-2}	

TABLE V. $|\Gamma_5|_{+1,m'}^{-1,m}$ values in Fig. 6.

$\lambda_j \backslash \lambda_i$	λ_5	λ_7	λ_9	λ_{11}
λ_6	0.110	0.452	0.334	0.601
λ_8	0.452	0.161	0.582	0.349
λ_{10}	0.334	0.582	0.323	0.366
λ_{12}	0.601	0.349	0.366	0.271

Appendix F.

Let us summarize the leakage pattern for would-be zero modes and that for non-zero modes. We first begin with the leakage pattern for the zero modes.

1. A zero mode of staggered fermions appears as a four-fold degenerate quartet. In other words, for the topological charge Q , the number of zero modes is $4 \times (n_+ + n_-)$, and $Q = n_- - n_+$ (Atiyah-Singer Index Theorem), where n_+ (n_-) is the number of right-handed (left-handed) zero mode quartets.
2. In the chirality $\Gamma_5 = [\gamma_5 \otimes 1]$ measurement, the zero mode has practically no leakage to other eigenstates.
3. In the shift $\Xi_5 = [1 \otimes \xi_5]$ measurement, the zero mode with eigenvalue λ has a full (100%) leakage into its parity partner mode with eigenvalue $-\lambda$, and no leakage into any other eigenmodes.

The leakage pattern for nonzero modes is

1. A non-zero mode of staggered fermions appears as an eight-fold degeneracy composed of a quartet ($+j$ quartet) and its parity partner quartet ($-j$ quartet). In other words, non-zero eigenmodes can be grouped into sets with eight elements in each set. This is due to the approximate $SU(4)$ taste symmetry and the conserved $U(1)_A$ axial symmetry.

2. In the chirality $\Gamma_5 = [\gamma_5 \otimes 1]$ measurement, the non-zero mode with eigenvalue $\lambda_{j,m}$ has no leakage to its own quartet (j quartet), but has leakage only to the parity partner ($-j$ quartet) with $\lambda_{-j,m'}$. It has no leakage to any eigenmode which belongs to other quartets with $\ell \neq \pm j$.

3. In the shift $\Xi_5 = [1 \otimes \xi_5]$ measurement, the non-zero mode with $\lambda_{j,m}$ has no leakage to its parity partner ($-j$ quartet) at all. But it has leakage only to the eigenstates in its own ($+j$) quartet. This pattern comes directly from the Ward identity. In other words, the Ξ_5 leakage pattern is a mirror image reflecting Γ_5 through the mirror of the Ward identity. Ξ_5 has no leakage to any eigenmode which belongs to other quartets with $\ell \neq \pm j$.

4. Thanks to the Ward identity of the conserved $U(1)_A$ symmetry, the leakage pattern of $|\Gamma_5|_{\ell,m'}^{-j,m}$ is identical to that of $|\Xi_5|_{\ell,m'}^{+j,m}$.

In Appendix E, we provide more examples to demonstrate our claim that the leakage pattern for zero modes holds in general. In Appendix F, we give more examples to demonstrate our claim that the leakage pattern for non-zero modes is valid in general. We have repeated numerical tests over hundreds of zero modes and tens of thousands of nonzero modes. We performed the numerical study on hundreds of gauge configurations and find that the above leakage pattern is valid for all of them except for those gauge configurations with unstable topological charge.

1. We find a number of gauge configurations which do not have a stable topological charge.
2. We find about 10 gauge configurations with unstable topological charge among 100 gauge configurations with 12^4 lattice geometry at $\beta = 4.6$.

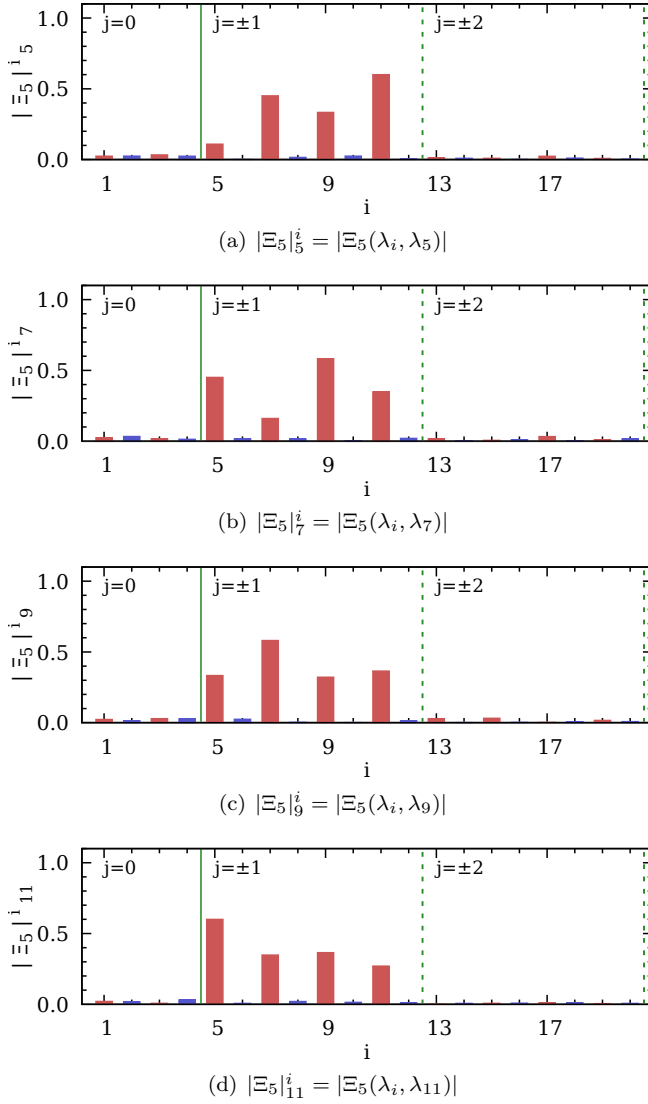


FIG. 7. $[1 \otimes \xi_5]$ leakage pattern for non-zero modes at $Q = -1$.

3. We find about 8 gauge configurations with unstable topological charge among 300 gauge configurations with 20^4 lattice geometry at $\beta = 5.0$.

TABLE VI. Numerical results for T_5 . To obtain the results, we use 292 gauge configurations with the input parameters in Table I. N_q represents the number of quartets used to obtain the statistical error. Here $j = 0$ represents would-be zero modes, and $j > 0$ represents non-zero modes.

j	$ \text{Re}(T_5) $	$ \text{Im}(T_5) $	N_q
$j = 0$	$7.2(130) \times 10^{-4}$	$5.9(46) \times 10^{-12}$	490
$j > 0$	$6.2(120) \times 10^{-3}$	$3.3(25) \times 10^{-12}$	7034

In Table VI, we present results for T_5 defined in Eq. (92), which is a direct barometer to estimate the effect of taste symmetry breaking. If the taste symmetry

is exactly conserved, then T_5 must vanish. Hence, a non-trivial value of T_5 indicates the size of taste symmetry breaking. In Table VI, we find that $|\text{Re}(T_5)|$ is of order 10^{-3} , while $|\text{Im}(T_5)|$ is essentially zero. This indicates that the effect of taste symmetry breaking is very small (in the sub-percent level within each quartet).

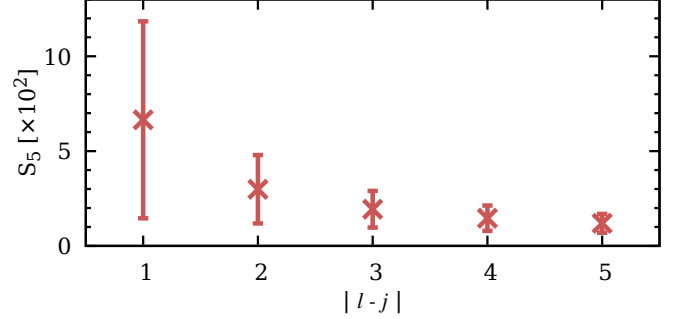


FIG. 8. S_5 as a function of $|\ell - j|$. Numerical values are given in Table VII.

In Fig. 8, we present S_5 defined in Eq. (93) as a function of $|\ell - j|$ with $\ell, j \geq 0$. Here $|\ell - j| = 1$ represents a pair of nearest neighbor quartets, $|\ell - j| = 2$ represents a pair of next-to-nearest neighbor quartets, and so on. The values of S_5 are the same size as the statistical errors. This indicates that the taste symmetry breaking results in simply random noise added to the physical signal ($S_5 = 0$). For $|\ell - j| = 1$, the noise is $\approx 7\%$, and for $|\ell - j| = 2$, the noise is $\approx 3\%$. We find that the noise decreases as $|\ell - j|$ increases. The numerical values of S_5 in Fig. 8 are presented in Table VII.

TABLE VII. Numerical results for S_5 . Here, we measure S_5 between two different quartets ($\ell \neq j$ and $\ell, j \geq 0$). N_p represents the number of (ℓ, j) pairs with $\ell \neq j$.

$ \ell - j $	S_5	N_p
1	$6.6(52) \times 10^{-2}$	7185
2	$3.0(18) \times 10^{-2}$	6893
3	$1.9(10) \times 10^{-2}$	6601
4	$1.5(7) \times 10^{-2}$	6309
5	$1.2(5) \times 10^{-2}$	6017

VI. MACHINE LEARNING

In previous sections, we have shown that the $U(1)_A$ symmetry of staggered fermions induces the chiral Ward identities in Eq. (78), and we have also noted that the approximate $SU(4)$ taste symmetry brings in the quartet behavior of the eigenvalue spectrum. Furthermore, a combined effect of those symmetries gives us distinctive leakage patterns for the chirality operator Γ_5 and the shift operator Ξ_5 . In this section, we apply a machine learning technique to the following tasks.

1. We want to know how much the non-zero modes respect the quartet classification rules, which come from the $SU(4)$ taste symmetry.
2. We want to know how efficiently we can measure the topological charge Q using the index theorem from the quartet structure of the non-zero modes.
3. We want to detect any anomalous behavior of the eigenvalue spectrum, which does not follow the standard leakage pattern of the non-zero modes.
4. We want to figure out what causes the anomalous behavior of the eigenvalue spectrum.

Let us explain our sampling method for the machine learning. In Fig. 9, we show matrix elements $|\Gamma_5|_j^i$ on a gauge configuration with $Q = 2$. Fig. 9(a) is for the 200 lowest eigenmodes, and Fig. 9(b) is a zoomed-in version of Fig. 9(a) for the 32 lowest eigenmodes. Here the depth of the blue color represents the size of the matrix element $|\Gamma_5|_j^i$, and i, j run from zero to 199. We identify two zero mode quartets (red boxes) by looking at the magnitude of the diagonal components. These two quartets have the same chirality ($n_- = 2$), which is consistent with the topological charge $Q = 2$. Excluding the would-be zero modes, we randomly choose a 15×15 sub-matrix of $|\Gamma_5|_j^i$ along the diagonal line of $|\Gamma_5|_j^i$ matrix elements. This 15×15 sub-matrix is the smallest square sub-matrix of $|\Gamma_5|$ which contains all elements of only one quartet of non-zero modes and its parity partner quartet.

In Fig. 10, we present 8 different classes for arbitrary samples. Our purpose for the machine learning is to find borders (black lines) of the non-zero mode quartets (or octets when the parity partners are included) in each sample. We classify arbitrary samples into eight different classes according to the location of the border lines. Each class is labeled as in Fig. 10.

TABLE VIII. Parameters for machine learning.

parameters	values
number of training configurations	120
number of training samples	1223
number of validation configurations	30
number of validation samples	308
number of test configurations	142
number of test samples	1448
loss function	categorical cross-entropy [43, 44]
optimization method	Adam [45]
activation function for hidden layers	ReLU [43]
activation function for output layer	softmax [43]

We use a deep learning model which combines the multi-layer perceptron (MLP) [43] and the convolutional neural network (CNN) [43]. In Table VIII, we present our basic setup for the machine learning. We use the

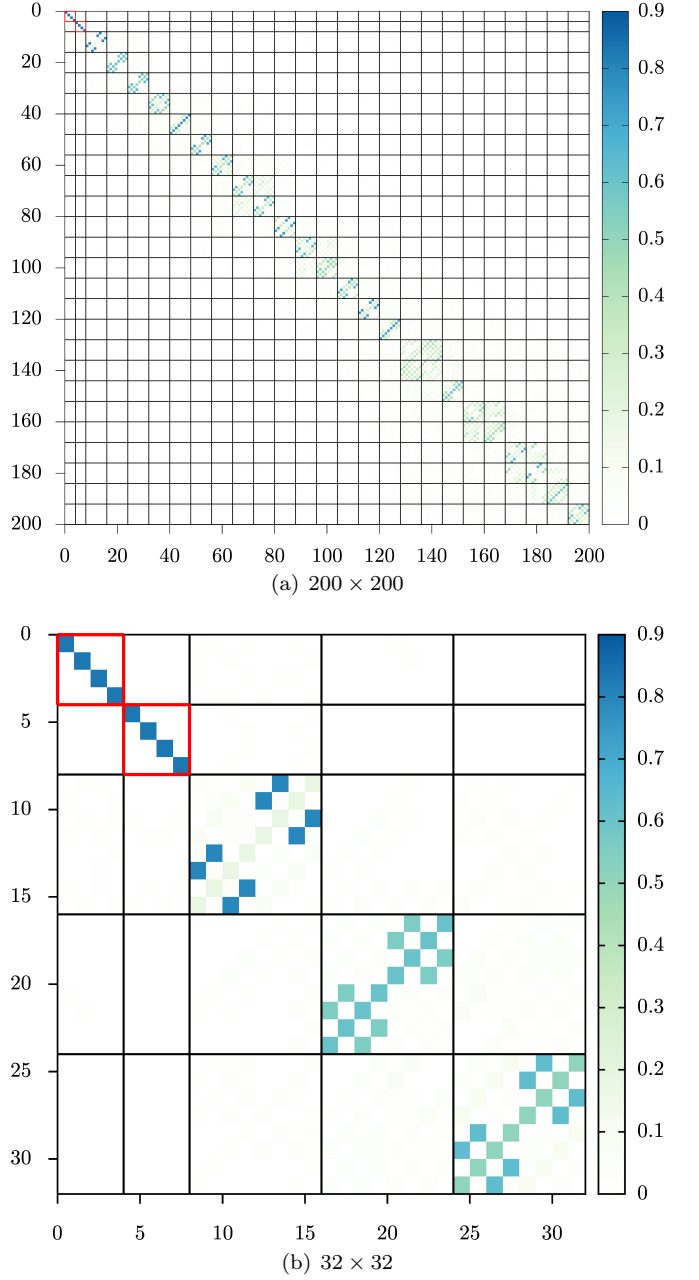


FIG. 9. Matrix elements of $|\Gamma_5|$ for 200 and 32 of the lowest eigenmodes on a gauge configuration with $Q = 2$. Here, indices on both axes are the eigenvalue index. The color of each square represents the magnitude of the corresponding matrix element. Black lines indicate borders of non-zero mode quartets, and red lines are those of zero mode quartets.

gauge configuration ensemble described in Table I. The data measured over 292 gauge configurations are distributed over a training set, validation set, and test set as in Table VIII. For each gauge configuration, we generate around ten 15×15 matrix samples from the 200 lowest eigenmodes without overlapping. We make popu-

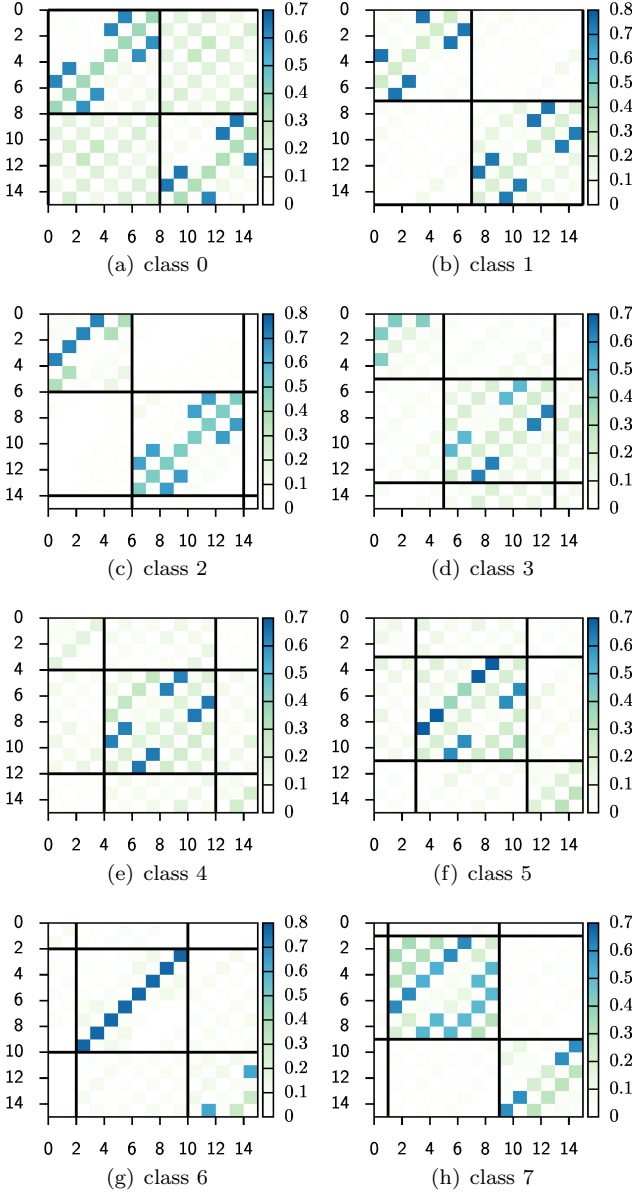


FIG. 10. Examples for our samples. Every sample contains only one non-zero mode quartet. There are eight kinds of classes according to the location of the borders of the quartet.

lar and suitable choices for the loss function¹, optimization method², and activation functions³ relevant to our purpose, which are summarized in Table VIII. The best

¹ Popular and basic loss functions such as the mean squared error (MSE) and mean absolute error (MAE) are usually used for regression problems. On the contrary, the categorical cross-entropy loss function is most applicable to multi-class classification problems.

² Popular optimization methods available in the market are stochastic gradient descent, AdaGrad, RMSprop, and Adam [45].

³ Popular activation functions are the tanh, sigmoid, and ReLU. Here, we make use of ReLU for the hidden layers since it is the

TABLE IX. Hyper-parameters for neural networks. Here, we show one of the examples of best performance, in which we use only MLP but not CNN.

layer	type	number of units	activation
input	-	225	-
hidden #1	MLP	160	ReLU
hidden #2	MLP	1210	ReLU
hidden #3	MLP	1490	ReLU
output	MLP	8	Softmax

hyper-parameters such as the number of layers and the number of units for each layer are determined by using the Keras Tuner [44].

The accuracy of classification per gauge configuration is obtained by averaging the accuracies of the machine learning (ML) prediction for all the samples on a single gauge configuration. Our best model achieves an average accuracy of 96.5(156)% for 142 test gauge configurations. The hyper-parameters which represent the structure of the neural network model are given in Table IX. Among the test set, we find five gauge configurations on which the average accuracy per gauge configuration is lower than 50%. Data show that some ghost (unphysical) eigenvectors are present in the eigenvalue spectrum on these gauge configurations, so that the ML prediction gives a wrong answer not due to failure of the ML algorithm but due to human mistakes in labeling quartet samples based on the eigenvalue index. Excluding these five gauge configurations, we achieve the average accuracy of 99.4(23)%. Considering that all samples generated on the same gauge configuration are connected by the eigenvalue index (or quartet index), this average accuracy of 99.4% implies that one can in the end find completely correct quartet groups for all the normal gauge configurations of the test set. It also demonstrates our claim that the leakage pattern is universal over all normal gauge configuration ensembles. Details of the results of this ML research will be reported separately in Ref. [46].

VII. ZERO MODES AND RENORMALIZATION

As explained in Sec. V, we know that there is practically no leakage for the zero modes in the chirality measurement. Hence, it is possible to determine the renormalization factor κ_P by imposing the index theorem as follows. For $Q \neq 0$,

$$4 \times Q = -\kappa_P \times \sum_{\lambda \in S_0} \langle f_\lambda^s | [\gamma_5 \otimes 1] | f_\lambda^s \rangle \quad (96)$$

simplest and fastest. The softmax function is essential for the output layer of the multi-class classification.

$$\kappa_P = -\frac{4Q}{C_0} \quad (97)$$

$$C_0 = \sum_{\lambda \in S_0} \Gamma_5(\lambda, \lambda) \quad (98)$$

where S_0 is the entire set of zero modes, and

$$\kappa_P = \frac{Z_{P \times S}(\mu)}{Z_{P \times P}(\mu)}, \quad (99)$$

where

$$O_S = \bar{\chi}[\gamma_5 \otimes 1]\chi \quad (100)$$

$$O_P = \bar{\chi}[\gamma_5 \otimes \xi_5]\chi \quad (101)$$

$$[O_S]_R(\mu) = Z_{P \times S}(\mu)[O_S]_B \quad (102)$$

$$[O_P]_R(\mu) = Z_{P \times P}(\mu)[O_P]_B, \quad (103)$$

and the subscript $[\dots]_R$ ($[\dots]_B$) represents a renormalized (bare) operator. The $Z_{P \times S}$ and $Z_{P \times P}$ are the renormalization factors for the bilinear operators O_S and O_P , respectively. One advantage of this scheme is that κ_P is independent of valence quark masses, even though we perform the measurement with arbitrary masses for valence quarks. Numerical results for κ_P are summarized in Table X.

There are a few key issues in the physical interpretation of κ_P .

- Since the topological charge Q and sum C_0 are independent of renormalization scale, κ_P must be independent of the renormalization scale μ .
- This means that the scale dependence of $Z_{P \times S}(\mu)$ must cancel off that of $Z_{P \times P}(\mu)$.
- It would be nice to cross-check this property of κ_P in the RI-MOM scheme [47] and in the RI-SMOM scheme [48].

TABLE X. Numerical results for κ_P .

topological charge	number of samples	κ_P
$ Q = 1$	72	1.26(13)
$ Q = 2$	68	1.22(3)
$ Q = 3$	45	1.23(2)
weighted average	241	1.23(2)

VIII. CONCLUSION

We study general properties of the eigenvalue spectrum of Dirac operators in the staggered fermion formalism. As an example, we use the Dirac operator for HYP staggered quarks. In Section V, we introduce a new chirality operator Γ_5 and a new shift operator Ξ_5 and prove that they respect the continuum recursion relationships, as

given in Eqs. (53)-(56) and Eqs. (60)-(61). Using these operators with nice chiral properties, we find that the leakage pattern of $|\Gamma_5|_{\ell, m'}^{j, m}$ is related to that of $|\Xi_5|_{\ell, m'}^{j, m}$ through the Ward identity of the conserved $U(1)_A$ symmetry.

We find that the leakage pattern of Γ_5 and Ξ_5 for the zero modes is quite different from that for the non-zero modes. This difference in leakage pattern allows us to distinguish the zero modes from the non-zero modes even though we do not know *a priori* about the topological charge. We find that using the leakage pattern of Γ_5 and Ξ_5 , one can determine the topological charge as reliably as when using standard field theoretical methods such as the cooling method.

We use a machine learning (ML) technique to check the universality of this leakage pattern over the entire ensemble of gauge configurations (refer to Table I). Our best-trained deep learning model identifies the quartet of non-zero modes with 98.7(34)% accuracy using a single normal gauge configuration. Choosing the highest probability prediction of the ML and comparing the prediction with the known answer, we find that the ML can identify all quartet groups on an eigenvalue spectrum correctly. In addition, the ML technique detects wrong answers resulting from human input mistakes since the ML prediction disagrees with a wrong answer by giving the prediction with low accuracy ($< 50\%$). This reassures us that the ML technique is highly reliable at identifying anomalous gauge configurations with defects such as violation of the index theorem and ghost eigenmodes.

Once we identify the zero modes, it is also possible to determine the ratio of renormalization factors $\kappa_P = Z_{P \times S}(\mu)/Z_{P \times P}(\mu)$ from the chirality measurement of Γ_5 .

The leakage pattern is a new concept introduced in this paper. It can be used to study the low lying eigenvalue spectrum of staggered Dirac operators systematically. It helps us understand how to extract the taste symmetry and chiral symmetry from the staggered eigenvalue spectrum. The leakage pattern will help us to dig out related physics more efficiently, such as topological charge, index theorem, Banks-Casher relation, and non-perturbative renormalization.

ACKNOWLEDGMENTS

We would like to express sincere gratitude to Eduardo Follana for helpful discussion and providing his code to cross-check results of our code. We also thank Jon A. Bailey for helpful comments on the manuscript. We also thank Stephen R. Sharpe for helpful discussion. The research of W. Lee is supported by the Mid-Career Research Program (Grant No. NRF-2019R1A2C2085685) of the NRF grant funded by the Korean government (MOE). This work was supported by Seoul National University Research Grant in 2019. W. Lee would like to acknowledge the support from the KISTI supercomputing center through the strategic support program for

the supercomputing application research [No. KSC-2016-C3-0072, KSC-2017-G2-0009, KSC-2017-G2-0014, KSC-2018-G2-0004, KSC-2018-CHA-0010, KSC-2018-CHA-0043]. Computations were carried out in part on the DAVID supercomputer at Seoul National University.

Appendix A: Lanczos algorithm

Lanczos is a numerical algorithm for calculating eigenvalues and eigenvectors of a Hermitian matrix [21]. It transforms an $n \times n$ Hermitian matrix H to a tridiagonal matrix T through a unitary transformation Q , which is represented by

$$T = Q^\dagger H Q. \quad (\text{A1})$$

Here columns of Q are composed of basis vectors of the n th Krylov subspace $\mathcal{K}_n(H, b)$ generated by H and a starting vector b of our choice. Each iteration of Lanczos computes a column of Q and T in sequence. At the end, diagonalizing the tridiagonal matrix T yields eigenvalues and eigenvectors of H .

In principle, Lanczos is a direct method that takes n iterations to construct the $n \times n$ tridiagonal matrix T . However, since these columns of T are computed in order, a sequence of $m < n$ iterations also constructs an $m \times m$ tridiagonal matrix T' which is a submatrix of T . In practice, the real benefit of Lanczos is that eigenvalues of T' approximate eigenvalues of T . As iteration continues, and the size of the submatrix T' increases, eigenvalues of T' converge to eigenvalues of T . The convergence behavior is somewhat complicated. The eigenvalues converge to the largest, the smallest, or the most sparse eigenvalue first. The speed of convergence depends on the density of eigenvalues. The less dense, the faster the convergence.

In this paper, we make use of two popular improvement techniques of Lanczos: (1) implicit restart [49], and (2) polynomial acceleration with Chebyshev polynomials [50]. The implicit restart method gets rid of converged eigenvalues in the middle of the Lanczos iteration. It takes effect as if we restarted the Lanczos with a shifted matrix H' given by

$$H' \equiv H - \sum_i \lambda_i \mathcal{I}, \quad (\text{A2})$$

where λ_i are eigenvalues we want to remove. Then H' is still Hermitian but does not have such eigenvalues λ_i . Hence, Lanczos with H' converges to remaining eigenvalues faster. The implicit restarting procedure gives us a new submatrix, which has a dimension $((m-r) \times (m-r))$ reduced by the number of eigenvalues we have removed (r). Then we iterate Lanczos r times to refill the submatrix and restore the structure of the $m \times m$ matrix. We repeat the implicit restart to obtain a new submatrix of dimension $(m-r) \times (m-r)$, and so on. This procedure allows us to control the size of the submatrix, the computational cost, and the memory usage, while the

submatrix T' contains $(m-r)$ eigenmodes that are more precise (much closer to the true eigenmodes of the full matrix H) for each iteration.

A polynomial operation on a matrix changes the eigenvalue spectrum accordingly while retaining the eigenvectors. Since the polynomial of a Hermitian matrix is also Hermitian, Lanczos is still available to calculate its eigenvalues and eigenvectors. By choosing a proper polynomial, one can manipulate the density of the eigenvalue spectrum so that the convergence to the desired eigenvalues is accelerated. A Chebyshev polynomial is a popular choice for this purpose. Using the Chebyshev polynomial, we want to map the first region of eigenmodes of no interest to $[-1, 1]$ and map the second region of eigenmodes of our interest to $[-\infty, -1]$. In the interval $[-1, 1]$, the eigenvalues are dense enough that Lanczos does not converge. In addition, the Chebyshev polynomial rapidly changes in the second region so that the density of eigenmodes is low enough to more quickly accelerate the convergence of Lanczos. Here we apply the Chebyshev polynomial for $D_s^\dagger D_s$, whose eigenvalues are $\lambda^2 \geq 0$. We set the lower bound of the first region to a value somewhat greater than the largest eigenvalue of interest. This strategy will not only suppress high unwanted eigenmodes, but also accelerate the speed of Lanczos for the low eigenmodes of interest.

Numerical stability is essential for the Lanczos algorithm. Each Lanczos iteration generates Lanczos vectors, which are column vectors of the unitary matrix Q in Eq. (A1). After several iterations, however, Lanczos vectors lose their orthogonality due to gradual loss of numerical precision. If not addressed, this loss would induce spurious ghost eigenvalues [51]. A straightforward prescription to solve the problem is performing a reorthogonalization for every calculation of Lanczos vectors. There are also alternative approaches to eliminate the ghost eigenvalues without reorthogonalization, such as the Cullum-Willoughby method [52, 53]. Here we choose the first solution and perform the full reorthogonalization for each Lanczos iteration.

For a large scale simulation using Lanczos, Multi-Grid Lanczos [54] and Block Lanczos [55] are available. Multi-Grid Lanczos is also based on the implicit restart and Chebyshev acceleration. In addition, Multi-Grid Lanczos reduces the memory requirement significantly by compressing the eigenvectors using their local coherence [56]. A spatially-blocked deflation subspace is constructed from some of the lowest eigenvectors of the Dirac operator. Then the coherence of eigenvectors allows us to represent other eigenvectors on this subspace and to run Lanczos with much less memory. Meanwhile, Block Lanczos utilizes the Split Grid method [55]. This algorithm deals with multiple starting vectors for Lanczos, where the Split Grid method divides the domain of the Dirac operator application into multiple smaller domains so that each partial domain runs in parallel on a partial grid (lattice) with a lower surface to volume ratio than that of the full grid. Hence, one can optimize the off-

node communication by adjusting the block (grid) size. This approach would give a significant speed-up compared with our method. We plan to implement Multi-Grid Lanczos and Block Lanczos in the near future.

Appendix B: Even-odd preconditioning and phase ambiguity

Even-odd preconditioning reorders a fermion field $\chi(x)$ so that even site fermion fields are obtained first, and odd site fermion fields are obtained from them:

$$\chi(x) = \begin{pmatrix} \chi_e \\ \chi_o \end{pmatrix}, \quad (\text{B1})$$

where χ_e (χ_o) is the fermion field collection on even (odd) sites. On this basis, the massless staggered Dirac operator D_s can be represented as a block matrix:

$$D_s = \begin{pmatrix} 0 & D_{eo} \\ D_{oe} & 0 \end{pmatrix}, \quad (\text{B2})$$

where D_{oe} (D_{eo}) relates even (odd) site fermion fields to odd (even) site fermion fields. Since $D_s^\dagger = -D_s$, we also find that $D_{oe}^\dagger = -D_{eo}$ and $D_{eo}^\dagger = -D_{oe}$.

On this basis, $D_s^\dagger D_s$ is expressed as

$$D_s^\dagger D_s = \begin{pmatrix} 0 & -D_{eo} \\ -D_{oe} & 0 \end{pmatrix} \begin{pmatrix} 0 & D_{eo} \\ D_{oe} & 0 \end{pmatrix} \quad (\text{B3})$$

$$= \begin{pmatrix} -D_{eo}D_{oe} & 0 \\ 0 & -D_{oe}D_{eo} \end{pmatrix}. \quad (\text{B4})$$

Hence, the eigenvalue equation of $D_s^\dagger D_s$ (Eq. (29)) can be divided into two eigenvalue equations as follows,

$$-D_{eo}D_{oe}|g_e\rangle = \lambda^2|g_e\rangle, \quad (\text{B5})$$

$$-D_{oe}D_{eo}|g_o\rangle = \lambda^2|g_o\rangle, \quad (\text{B6})$$

where $|g_{e(o)}\rangle$ is the collection of even (odd) site components of $|g_{\lambda^2}^s\rangle$. Here we omit the superscript s and the subscript λ^2 for notational simplicity. Now let us multiply D_{oe} from the left on both sides of Eq. (B5). Then we find that

$$-D_{oe}D_{eo}(D_{oe}|g_e\rangle) = \lambda^2(D_{oe}|g_e\rangle), \quad (\text{B7})$$

which is identical to Eq. (B6). Hence, we find that $|g_o\rangle = \eta D_{oe}|g_e\rangle$ where $\eta = re^{i\alpha}$ is an arbitrary complex number with $r > 0$ and $0 \leq \alpha < 2\pi$. Here r represents the scaling behavior and α represents a random phase. Since $-D_{eo}D_{oe}(=D_{oe}^\dagger D_{oe})$ is Hermitian and positive semi-definite, one can solve Eq. (B5) using the Lanczos algorithm introduced in Appendix A. From the result for $|g_e\rangle$, it is straightforward to obtain the eigenvector $|g_{\lambda^2}^s\rangle$ of Eq. (29) since

$$|g_{\lambda^2}^s\rangle = \begin{pmatrix} |g_e\rangle \\ \eta D_{oe}|g_e\rangle \end{pmatrix}. \quad (\text{B8})$$

Now we apply the projection operator P_+ , defined in Eq. (32), to $|g_{\lambda^2}^s\rangle$. Using Eq. (B5), we find that

$$\begin{aligned} |\chi_+\rangle &= P_+|g_{\lambda^2}^s\rangle = \begin{pmatrix} i\lambda & D_{eo} \\ D_{oe} & i\lambda \end{pmatrix} \begin{pmatrix} |g_e\rangle \\ \eta D_{oe}|g_e\rangle \end{pmatrix} \\ &= (1 + i\eta\lambda) \begin{pmatrix} i\lambda|g_e\rangle \\ D_{oe}|g_e\rangle \end{pmatrix}. \end{aligned} \quad (\text{B9})$$

Similarly, for the projection operator P_- , defined in Eq. (33), we find that

$$|\chi_-\rangle = P_-|g_{\lambda^2}^s\rangle = (1 - i\eta\lambda) \begin{pmatrix} -i\lambda|g_e\rangle \\ D_{oe}|g_e\rangle \end{pmatrix}. \quad (\text{B10})$$

Since η only appears in the overall factor for both cases, it gives only the relative phase difference between the normalized eigenvectors $|f_{\pm\lambda}^s\rangle$ defined in Eqs. (36) and (37).

We can proceed further to obtain the eigenvectors $|f_{\pm\lambda}^s\rangle$. The norm of $|\chi_+\rangle$ is given by

$$\langle\chi_+|\chi_+\rangle = [(1 - i\eta^*\lambda)(1 + i\eta\lambda)] \cdot 2\lambda^2\langle g_e|g_e\rangle. \quad (\text{B11})$$

Hence, $|f_{+\lambda}^s\rangle$ is

$$|f_{+\lambda}^s\rangle = \frac{1}{N} \sqrt{\frac{1 + i\eta\lambda}{1 - i\eta^*\lambda}} \begin{pmatrix} i\lambda|g_e\rangle \\ D_{oe}|g_e\rangle \end{pmatrix}, \quad (\text{B12})$$

where

$$N \equiv \sqrt{2\lambda^2\langle g_e|g_e\rangle}. \quad (\text{B13})$$

Similarly,

$$|f_{-\lambda}^s\rangle = \frac{1}{N} \sqrt{\frac{1 - i\eta\lambda}{1 + i\eta^*\lambda}} \begin{pmatrix} -i\lambda|g_e\rangle \\ D_{oe}|g_e\rangle \end{pmatrix}. \quad (\text{B14})$$

These results for $|f_{\pm\lambda}^s\rangle$ indicate that the phase difference θ for the Γ_ϵ transformation defined in Eq. (47) depends on the value of η .

In our numerical study, we set η to $\eta = re^{i\alpha} = 1$: $r = 1$ and $\alpha = 0$. Hence, the relative random phase between $|f_{\pm\lambda}^s\rangle$ states is removed by hand. Therefore, our value of θ defined in Eq. (47) includes a bias from our choice of $\eta = 1$.

For $\eta = 1$ (our choice), $\Gamma_\epsilon|f_{+\lambda}^s\rangle$ is

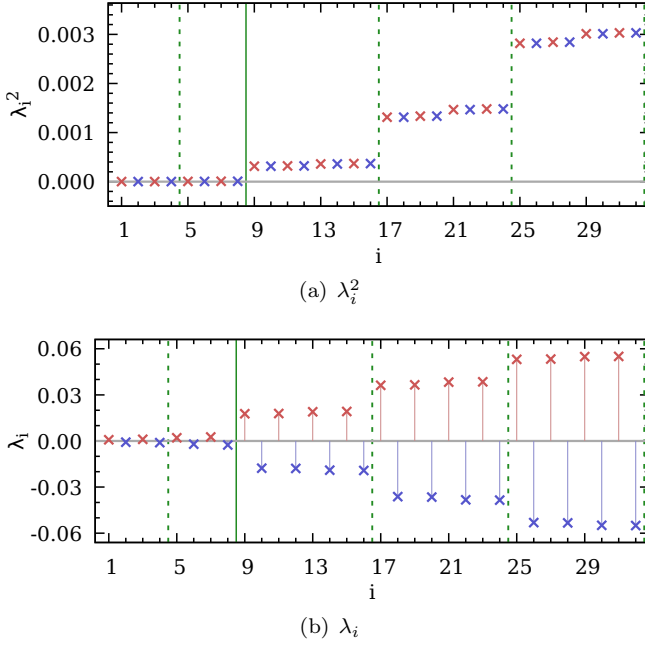
$$\Gamma_\epsilon|f_{+\lambda}^s\rangle = \frac{1}{N} \sqrt{\frac{1 + i\lambda}{1 - i\lambda}} \begin{pmatrix} i\lambda|g_e\rangle \\ -D_{oe}|g_e\rangle \end{pmatrix}, \quad (\text{B15})$$

while $|f_{-\lambda}^s\rangle$ is

$$|f_{-\lambda}^s\rangle = \frac{1}{N} \sqrt{\frac{1 - i\lambda}{1 + i\lambda}} \begin{pmatrix} -i\lambda|g_e\rangle \\ D_{oe}|g_e\rangle \end{pmatrix}. \quad (\text{B16})$$

Then we obtain $e^{i\theta}$ from the following matrix element,

$$\langle f_{-\lambda}^s | \Gamma_\epsilon | f_{+\lambda}^s \rangle = \frac{1}{N^2} \sqrt{\left(\frac{1 - i\lambda}{1 + i\lambda} \right)^* \frac{1 + i\lambda}{1 - i\lambda}} \cdot (-N^2)$$

FIG. 11. The same as Fig. 1 except for $Q = -2$.

$$\begin{aligned}
 &= -\frac{1+i\lambda}{1-i\lambda} \\
 &= e^{i(\pi+2\beta)} = e^{i\theta}, \quad (B17)
 \end{aligned}$$

where $\beta \equiv \arctan(\lambda)$. From Eqs. (47) and (B17), we find that

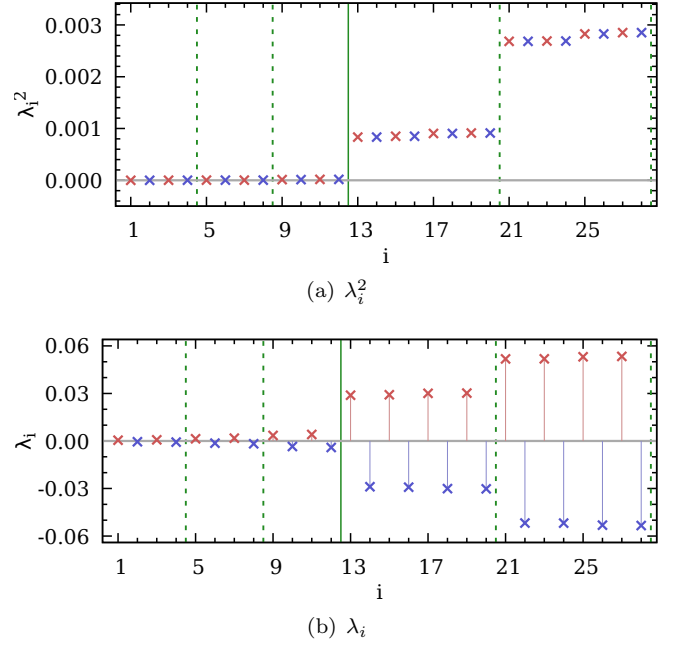
$$\theta = \pi + 2\beta. \quad (B18)$$

In Fig. 3, we show the measurements of the phase θ for hundreds of eigenvectors on a gauge configuration with $Q = -1$. The results for θ are consistent with our theoretical prediction Eq. (B18) within numerical precision.

Appendix C: Eigenvalue spectrum for $Q = -2$ and $Q = -3$

In Figs. 11 and 12, we present examples of the eigenvalue spectrum for $Q = -2$ and $Q = -3$, respectively. Figures 11(a) and 12(a) show eigenvalues λ^2 for the eigenvectors $|g_{\lambda^2}^s\rangle$ defined in Eq. (29). In Fig. 11, we find two sets of four-fold degenerate eigenstates, corresponding to $\{\lambda_1, \lambda_2, \lambda_3, \lambda_4\}$ and $\{\lambda_5, \lambda_6, \lambda_7, \lambda_8\}$. Each set of four eigenvalues indicates a quartet of would-be zero modes. The number of quartets is related to the topological charge $Q = -2$ by the index theorem of Eq. (23) when all would-be zero modes have the same chirality ($n_- = 0$ and $n_+ = 2$). Apart from the would-be zero modes, we observe that non-zero modes are eight-fold degenerate, as in the cases $Q = 0$ (Fig. 1) and $Q = -1$ (Fig. 2).

Similarly, in Fig. 12, we find three quartets of would-be zero modes with $n_- = 0$ and $n_+ = 3$ ($Q = -3$): $\{\lambda_1, \lambda_2, \lambda_3, \lambda_4\}$, $\{\lambda_5, \lambda_6, \lambda_7, \lambda_8\}$, and $\{\lambda_9, \lambda_{10}, \lambda_{11}, \lambda_{12}\}$.

FIG. 12. The same as Fig. 1 except for $Q = -3$.

Because the number of quartets equals the absolute value of the topological charge $|Q| = 3$, it is possible to deduce that all the would-be zero modes have the same chirality in accordance with the index theorem of Eq. (23). For non-zero modes, we observe the pattern of eight-fold degeneracy as in other examples for $Q = 0$ in Fig. 1, $Q = -1$ in Fig. 2, and $Q = -2$ in Fig. 11.

Appendix D: Recursion relationships for chirality operators

We define the chirality operator

$$\langle f_\alpha^s | [\gamma_5 \otimes 1] | f_\beta^s \rangle \equiv \int d^4x [f_\alpha^s(x_A)]^\dagger (\gamma_5 \otimes 1)_{AB} U(x_A, x_B) f_\beta^s(x_B) \quad (D1)$$

$$\overline{(\gamma_S \otimes \xi_T)}_{AB} = \frac{1}{4} \text{Tr}(\gamma_A^\dagger \gamma_S \gamma_B \gamma_T^\dagger) \quad (D2)$$

$$U(x_A, x_B) = \mathbb{P}_{SU(3)} \left[\sum_{p \in C} V(x_A, x_{p_1}) V(x_{p_1}, x_{p_2}) V(x_{p_2}, x_{p_3}) V(x_{p_3}, x_B) \right] \quad (D3)$$

First let us prove the following theorem.

Theorem D.1.

$$[\gamma_5 \otimes 1][\gamma_5 \otimes 1] = [1 \otimes 1] \quad (D4)$$

Proof. Let us first rewrite $[\gamma_5 \otimes 1]^2$ as follows,

$$[\gamma_5 \otimes 1]_{AC}^2 = \sum_B \overline{(\gamma_5 \otimes 1)}_{AB} U(x_A, x_B)$$

$$\begin{aligned}
& \cdot \overline{(\gamma_5 \otimes 1)}_{BC} U(x_B, x_C) \\
&= \sum_B [\overline{(\gamma_5 \otimes 1)}_{AB} \overline{(\gamma_5 \otimes 1)}_{BC}] \\
& \cdot [U(x_A, x_B) U(x_B, x_C)] \quad (D5)
\end{aligned}$$

We know that

$$\begin{aligned}
\overline{(\gamma_5 \otimes 1)}_{AB} &= \frac{1}{4} \text{Tr}(\gamma_A^\dagger \gamma_5 \gamma_B 1) \\
&= \delta_{B\bar{A}} [\eta_1(A) \eta_2(A) \eta_3(A) \eta_4(A)] \\
&= \delta_{B\bar{A}} \eta_5(A), \quad (D6)
\end{aligned}$$

where $\bar{A}_\mu = (A_\mu + 1) \bmod 2$, and

$$\eta_\mu(A) = (-1)^{X_\mu}, \quad \text{for } \mu = 1, 2, 3, 4, \quad (D7)$$

$$X_\mu = \sum_{\nu < \mu} A_\nu, \quad (D8)$$

$$\eta_5(A) = \eta_1(A) \eta_2(A) \eta_3(A) \eta_4(A) = (-1)^{A_1 + A_3}. \quad (D9)$$

Similarly, we find that

$$\overline{(\gamma_5 \otimes 1)}_{BC} = \delta_{C\bar{B}} \eta_5(B). \quad (D10)$$

Hence, we can rewrite Eq. (D5) as follows,

$$\begin{aligned}
[\gamma_5 \otimes 1]_{AC}^2 &= \sum_B [\delta_{B\bar{A}} \eta_5(A) \delta_{C\bar{B}} \eta_5(B)] \\
& \cdot [U(x_A, x_B) U(x_B, x_C)] \\
&= \delta_{AC} [U(x_A, x_{\bar{A}}) U(x_{\bar{A}}, x_A)], \quad (D11)
\end{aligned}$$

where we use the helpful identity $\eta_5(\bar{A}) = \eta_5(A)$. Thanks to the $SU(3)$ projection in Eq. (D3), $U(x_{\bar{A}}, x_A) = [U(x_A, x_{\bar{A}})]^\dagger \in SU(3)$. Hence, $[U(x_A, x_{\bar{A}}) U(x_{\bar{A}}, x_A)] = 1$. Therefore, we can rewrite Eq. (D11) as follows,

$$[\gamma_5 \otimes 1]_{AC}^2 = \delta_{AC} = [1 \otimes 1]_{AC}. \quad (D12)$$

Hence, we have just proven that $[\gamma_5 \otimes 1]^2 = [1 \otimes 1]$. (Q.E.D.) \square

Using the results of Eq. (D4), we can prove the recursion relationship as follows,

$$[\gamma_5 \otimes 1]^{2n+1} = ([\gamma_5 \otimes 1]^2)^n \cdot [\gamma_5 \otimes 1] \quad (D13)$$

$$= ([1 \otimes 1])^n \cdot [\gamma_5 \otimes 1] \quad (D14)$$

$$= [1 \otimes 1] \cdot [\gamma_5 \otimes 1] \quad (D15)$$

$$= [\gamma_5 \otimes 1]. \quad (D16)$$

Using the results of Eq. (D4), we can prove another recursion relationship as follows,

$$[\gamma_5 \otimes 1]^{2n} = ([\gamma_5 \otimes 1]^2)^n \quad (D17)$$

$$= ([1 \otimes 1])^n \quad (D18)$$

$$= [1 \otimes 1]. \quad (D19)$$

Finally, we can prove the following theorem.

Theorem D.2.

$$[\frac{1+\gamma_5}{2} \otimes 1] [\frac{1+\gamma_5}{2} \otimes 1] = [\frac{1+\gamma_5}{2} \otimes 1] \quad (D20)$$

Proof.

$$\begin{aligned}
[\frac{1+\gamma_5}{2} \otimes 1]^2 &= \frac{1}{4} ([1 \otimes 1] + [\gamma_5 \otimes 1])^2 \\
&= \frac{1}{4} ([1 \otimes 1] + 2[\gamma_5 \otimes 1] + [\gamma_5 \otimes 1]^2) \\
&= \frac{1}{2} ([1 \otimes 1] + [\gamma_5 \otimes 1]) \\
&= [\frac{1+\gamma_5}{2} \otimes 1]. \quad (D21)
\end{aligned}$$

(Q.E.D.) \square

Using Eq. (D20), we can prove that for integer $n > 0$,

$$[\frac{1+\gamma_5}{2} \otimes 1]^n = [\frac{1+\gamma_5}{2} \otimes 1] \quad (D22)$$

by induction.

At this stage, it will be trivial to prove that

$$[\frac{1+\gamma_5}{2} \otimes 1] [\frac{1-\gamma_5}{2} \otimes 1] = 0. \quad (D23)$$

Appendix E: Examples for the leakage pattern of zero modes

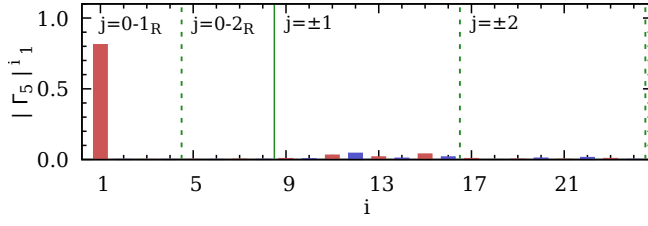
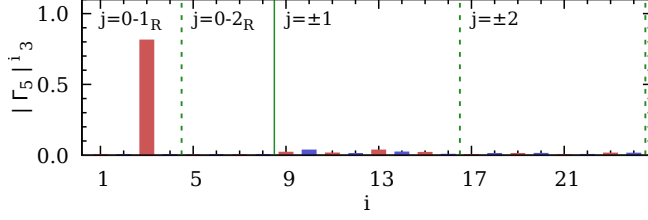
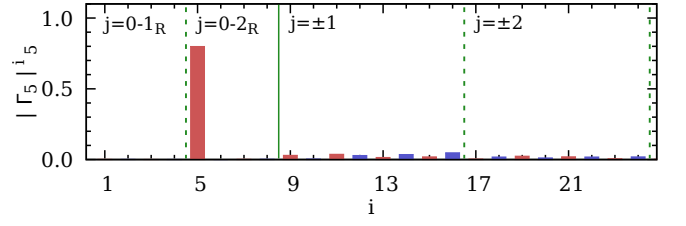
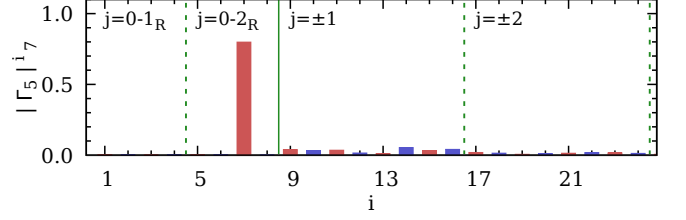
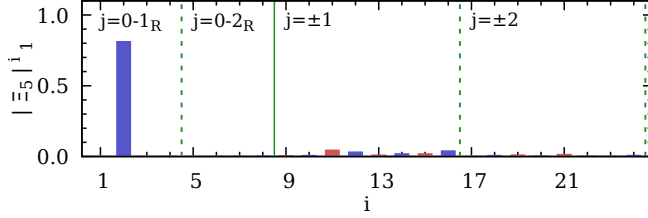
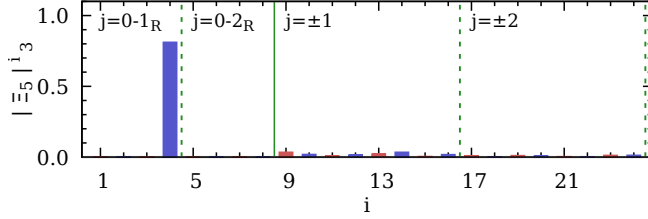
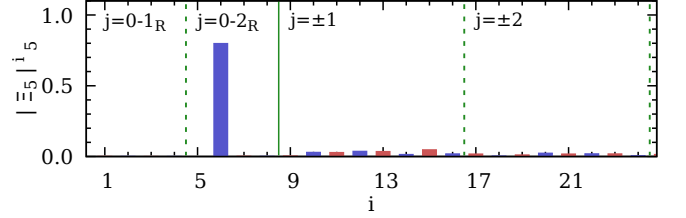
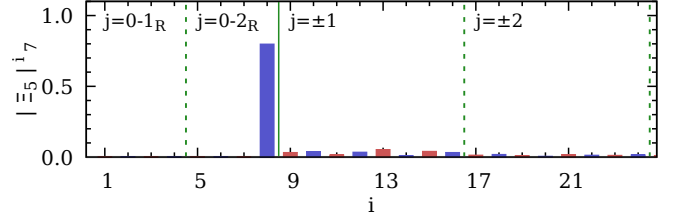
Let us begin with the case $Q = -2$. In Fig. 13, we show leakage patterns of the chirality operator for the first set of zero modes at $Q = -2$. In Fig. 14, we present the leakage patterns of the shift operator for the first set of zero modes at $Q = -2$. By comparing Fig. 13 with Fig. 14, we find that the chiral Ward identities of Eqs. (78) and (79) are well-respected.

In Fig. 15, we show leakage patterns of the chirality operator for the second set of zero modes at $Q = -2$. In Fig. 16, we present the leakage patterns of the shift operator for the second set of zero modes at $Q = -2$. By comparing Fig. 15 with Fig. 16, we find that the chiral Ward identities of Eqs. (78) and (79) are well-preserved.

Now let us consider an example with $Q = -3$. The leakage patterns for the first and second sets of zero modes are similar to those at $Q = -2$. Hence, we choose the third set of zero modes as our example. In Fig. 17, we show leakage patterns of the chirality operator for the third set of zero modes at $Q = -3$. In Fig. 18, we present the leakage pattern of the shift operator for the third set of zero modes at $Q = -3$. By comparing Fig. 17 with Fig. 18, we find that the chiral Ward identities of Eqs. (78) and (79) are well-preserved.

Appendix F: Examples for the leakage pattern of non-zero modes

Let us begin with an example with $Q = 0$. Since the gauge configuration with $Q = 0$ usually has no zero

(a) $|\Gamma_5|_1^i = |\Gamma_5(\lambda_i, \lambda_1)|$ (b) $|\Gamma_5|_3^i = |\Gamma_5(\lambda_i, \lambda_3)|$ FIG. 13. $[\gamma_5 \otimes 1]$ leakage pattern for the first quartet of would-be zero modes at $Q = -2$.(a) $|\Gamma_5|_5^i = |\Gamma_5(\lambda_i, \lambda_5)|$ (b) $|\Gamma_5|_7^i = |\Gamma_5(\lambda_i, \lambda_7)|$ FIG. 15. $[\gamma_5 \otimes 1]$ leakage pattern for the second quartet of would-be zero modes at $Q = -2$.(a) $|\Xi_5|_1^i = |\Xi_5(\lambda_i, \lambda_1)|$ (b) $|\Xi_5|_3^i = |\Xi_5(\lambda_i, \lambda_3)|$ FIG. 14. $[1 \otimes \xi_5]$ leakage pattern for the first quartet of would-be zero modes at $Q = -2$.(a) $|\Xi_5|_5^i = |\Xi_5(\lambda_i, \lambda_5)|$ (b) $|\Xi_5|_7^i = |\Xi_5(\lambda_i, \lambda_7)|$ FIG. 16. $[1 \otimes \xi_5]$ leakage pattern for the second quartet of would-be zero modes at $Q = -2$.

mode ($n_- = n_+ = 0$), it is relatively easy to study non-zero modes. In Fig. 19, we present leakage patterns of the chirality operator $\Gamma_5 = [\gamma_5 \otimes 1]$ for non-zero modes $\{\lambda_1, \lambda_3, \lambda_5, \lambda_7\} = \{\lambda_{j,m} | j = +1, m = 1, 2, 3, 4\}$ in the $j = +1$ quartet when $Q = 0$. The results show that the Γ_5 leakages for non-zero modes $\lambda_{+1,m}$ mostly go into their parity partners $\{\lambda_2, \lambda_4, \lambda_6, \lambda_8\} = \{\lambda_{j,m} | j = -1, m = 1, 2, 3, 4\}$ in the $j = -1$ quartet. Meanwhile, the leakages to other quartets such as $j = \pm 2, \pm 3$ are negligibly small compared to those of the $j = -1$ quartet elements. This observation is consistent with that for $Q = -1$ in Fig. 6.

In Fig. 20, we present leakage patterns of the shift operator $\Xi_5 = [1 \otimes \xi_5]$ for the non-zero modes $\{\lambda_1, \lambda_3, \lambda_5, \lambda_7\}$ of $\lambda_{+1,m}$ in the $j = +1$ quartet when $Q = 0$. For the Ξ_5

operator, we find the great part of leakages are from non-zero modes $\lambda_{+1,m}$ to other elements within the $j = +1$ quartet. Meanwhile, there are only negligible leakages to parity partner quartet elements ($j = -1$) and other quartets with $j = \pm 2, \pm 3$, and so on. This observation corresponds to the case $Q = -1$ in Fig. 7. We also find that the leakages of Γ_5 in Fig. 19 and Ξ_5 in Fig. 20 are related to each other by the Ward identity of Eq. (95).

In Figs. 21 and 22, we present leakage patterns of the Γ_5 and Ξ_5 operators, respectively, for non-zero modes $\{\lambda_9, \lambda_{11}, \lambda_{13}, \lambda_{15}\} = \{\lambda_{j,m} | j = +2, m = 1, 2, 3, 4\}$ in the $j = +2$ quartet when $Q = 0$. Similar to the above cases for $j = +1$, Γ_5 leakages for non-zero modes of $j = +2$ mostly go to their parity partner quartet elements of $j =$

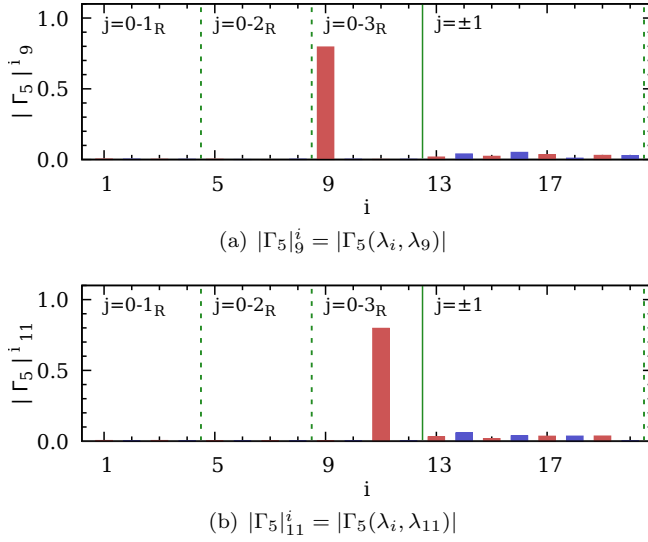


FIG. 17. $[\gamma_5 \otimes 1]$ leakage pattern for the third quartet of would-be zero modes at $Q = -3$.

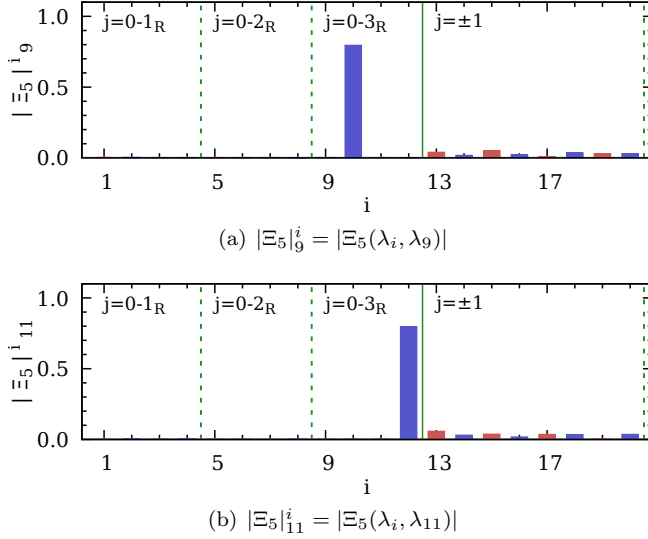


FIG. 18. $[1 \otimes \xi_5]$ leakage pattern for the third quartet of would-be zero modes at $Q = -3$.

-2 : $\{\lambda_{10}, \lambda_{12}, \lambda_{14}, \lambda_{16}\} = \{\lambda_{j,m} | j = -2, m = 1, 2, 3, 4\}$, and Ξ_5 leakages mostly go to members within the $j = +2$ quartet: $\{\lambda_9, \lambda_{11}, \lambda_{13}, \lambda_{15}\}$. There are only negligible leakages to other quartets for both operators.

Now let us examine the leakage patterns when would-be zero modes exist ($Q \neq 0$). In Figs. 23 and 24, we present leakage patterns of the Γ_5 and Ξ_5 operators, respectively, for non-zero modes $\{\lambda_9, \lambda_{11}, \lambda_{13}, \lambda_{15}\}$ in the $j = +1$ quartet when $Q = -2$. There are two quartets of right-handed would-be zero modes where $j = 0 - 1_R$ and $0 - 2_R$, which corresponds to $n_- = 0$ and $n_+ = 2$ with $Q = -2$ by the index theorem ($Q = n_- - n_+$).

As in the cases $Q = -1$ (Figs. 6 and 7) and $Q = 0$ (Figs. 19 and 20), Γ_5 leakages from non-zero modes of

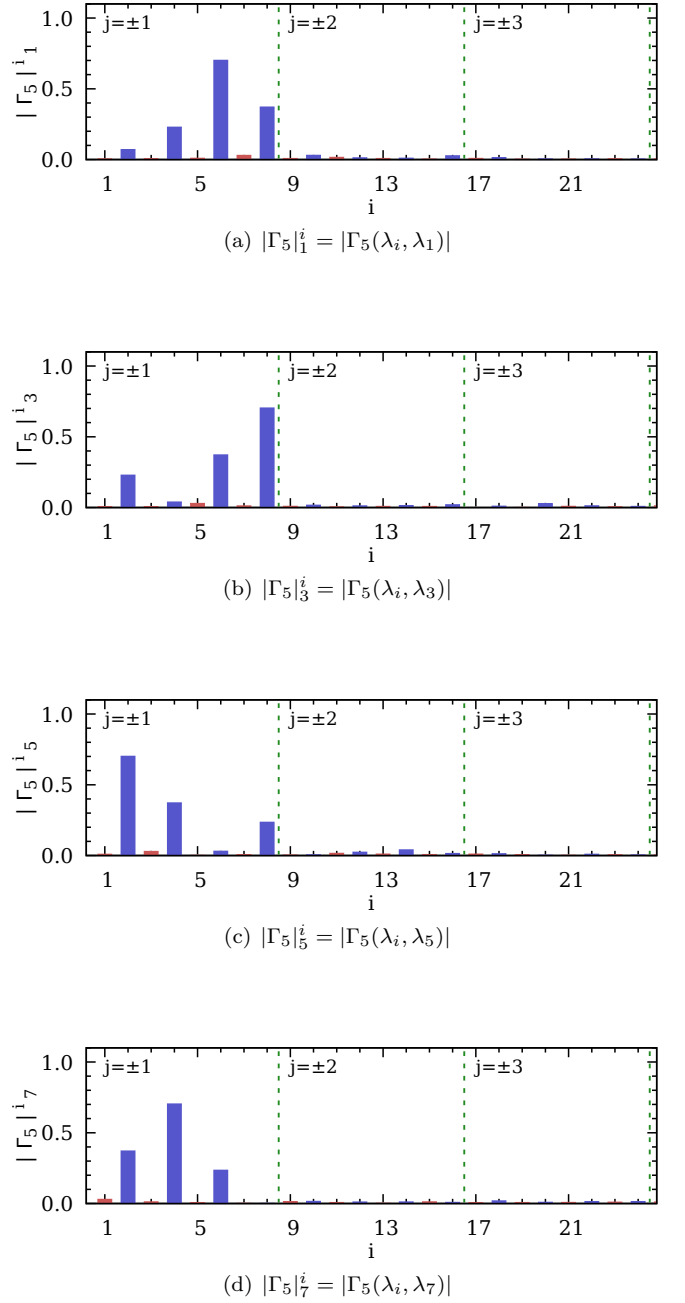


FIG. 19. $[\gamma_5 \otimes 1]$ leakage pattern for the first quartet of non-zero modes at $Q = 0$.

$j = +1$ mostly go to the parity partner $j = -1$ quartet, and Ξ_5 leakages from non-zero modes of $j = +1$ mostly go within the $j = +1$ quartet itself. Leakages to other non-zero mode quartets and would-be zero mode quartets are negligibly small. We also find that the Ward identity between the two leakage patterns holds.

In Figs. 25 and 26, we present leakage patterns for the Γ_5 and Ξ_5 operators, respectively, for non-zero modes $\{\lambda_{13}, \lambda_{15}, \lambda_{17}, \lambda_{19}\}$ in the $j = +1$ quartet when $Q = -3$. Their leakage patterns are also consistent with those for $Q = 0, -1, -2$ in our previous discussion.

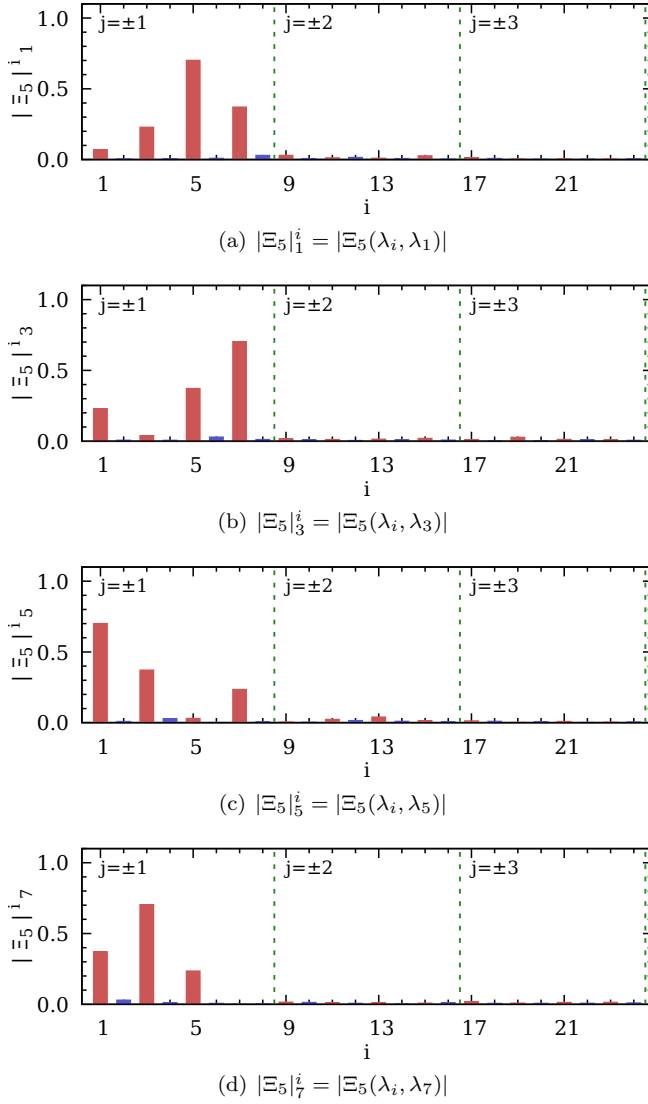


FIG. 20. $[1 \otimes \xi_5]$ leakage pattern for the first quartet of non-zero modes at $Q = 0$.

-
- [1] M. F. Atiyah and I. M. Singer, *Bull. Am. Math. Soc.* **69**, 422 (1963).
- [2] T. Banks and A. Casher, *Nucl. Phys.* **B169**, 103 (1980).
- [3] E. V. Shuryak and J. J. M. Verbaarschot, *Nucl. Phys.* **A560**, 306 (1993), arXiv:hep-th/9212088 [hep-th].
- [4] H. Leutwyler and A. V. Smilga, *Phys. Rev.* **D46**, 5607 (1992).
- [5] A. Hasenfratz and F. Knechtli, *Phys. Rev.* **D64**, 034504 (2001), arXiv:hep-lat/0103029 [hep-lat].
- [6] W.-j. Lee and S. R. Sharpe, *Phys. Rev.* **D66**, 114501 (2002), arXiv:hep-lat/0208018 [hep-lat].
- [7] E. Follana, Q. Mason, C. Davies, K. Hornbostel, G. P. Lepage, J. Shigemitsu, H. Trotter, and K. Wong (HPQCD, UKQCD), *Phys. Rev.* **D75**, 054502 (2007), arXiv:hep-lat/0610092 [hep-lat].
- [8] E. Follana, A. Hart, and C. T. H. Davies (HPQCD, UKQCD), *Phys. Rev. Lett.* **93**, 241601 (2004), arXiv:hep-lat/0406010 [hep-lat].
- [9] E. Follana, A. Hart, C. T. H. Davies, and Q. Mason (HPQCD, UKQCD), *Phys. Rev.* **D72**, 054501 (2005), arXiv:hep-lat/0507011 [hep-lat].
- [10] S. Durr, C. Hoelbling, and U. Wenger, *Phys. Rev.* **D70**, 094502 (2004), arXiv:hep-lat/0406027 [hep-lat].
- [11] V. Azcoiti, G. Di Carlo, E. Follana, and A. Vaquero, *Phys. Lett.* **B744**, 303 (2015), arXiv:1410.5733 [hep-lat].
- [12] S. Durr, *Phys. Rev.* **D87**, 114501 (2013), arXiv:1302.0773 [hep-lat].
- [13] D. H. Adams, *Phys. Rev. Lett.* **104**, 141602 (2010), arXiv:0912.2850 [hep-lat].
- [14] N. D. Cundy, H. Jeong, and W. Lee, *PoS LAT-TICE2015*, 066 (2016).
- [15] H. Jeong, S. Jwa, J. Kim, S. Kim, S. Lee, W. Lee, and

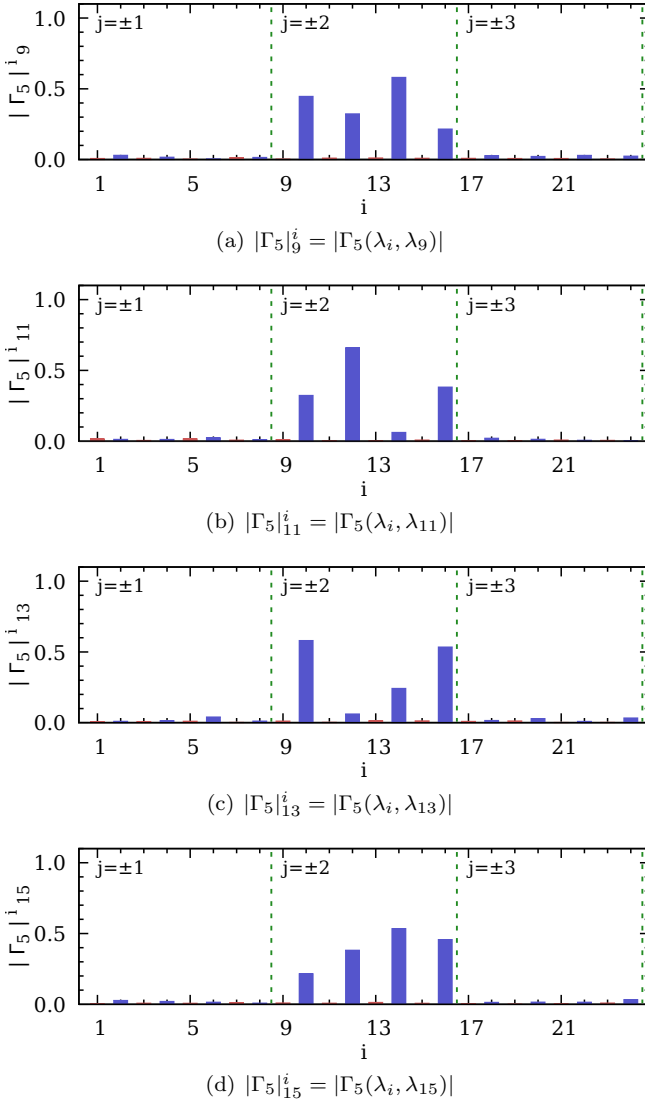


FIG. 21. $[\gamma_5 \otimes 1]$ leakage pattern for the second quartet of non-zero modes at $Q = 0$.

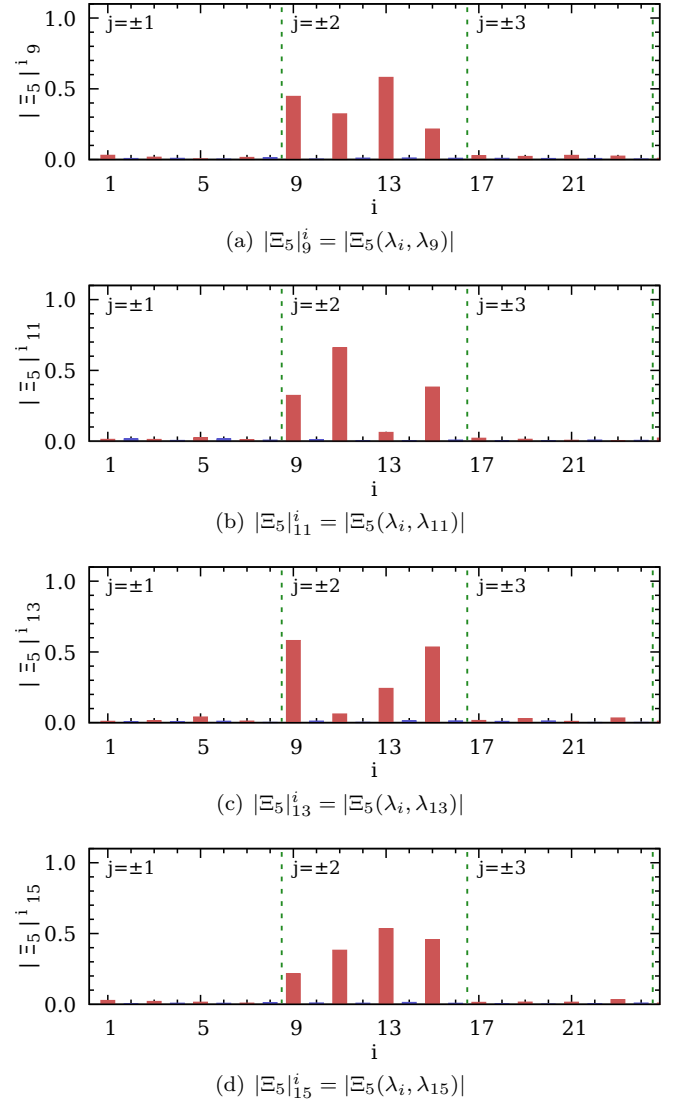


FIG. 22. $[1 \otimes \xi_5]$ leakage pattern for the second quartet of non-zero modes at $Q = 0$.

- J. Pak (SWME) (2017) arXiv:1711.01826 [hep-lat].
- [16] H. Jeong, C. Jung, S. Kim, W. Lee, and J. Pak (SWME), PoS **LATTICE2019**, 031 (2019), arXiv:2001.06568 [hep-lat].
- [17] S. Weinberg, *The quantum theory of fields. Vol. 2: Modern applications* (Cambridge University Press, 2013).
- [18] A. Bazavov *et al.* (MILC), Rev. Mod. Phys. **82**, 1349 (2010), arXiv:0903.3598 [hep-lat].
- [19] M. F. L. Golterman and J. Smit, Nucl. Phys. **B245**, 61 (1984).
- [20] W.-J. Lee and S. R. Sharpe, Phys. Rev. **D60**, 114503 (1999), arXiv:hep-lat/9905023 [hep-lat].
- [21] C. Lanczos, J. Res. Natl. Bur. Stand. B Math. Sci. **45**, 255 (1950).
- [22] T. A. DeGrand and P. Rossi, Comput. Phys. Commun. **60**, 211 (1990).
- [23] Y. Saad, Math. Comp. **42**, 567 (1984).
- [24] J. Smit and J. C. Vink, Nucl. Phys. **B286**, 485 (1987).
- [25] W.-j. Lee, Phys. Rev. **D66**, 114504 (2002), arXiv:hep-lat/0208032 [hep-lat].
- [26] K. Orginos, D. Toussaint, and R. L. Sugar (MILC), Phys. Rev. **D60**, 054503 (1999), arXiv:hep-lat/9903032 [hep-lat].
- [27] G. P. Lepage, Phys. Rev. **D59**, 074502 (1999), arXiv:hep-lat/9809157 [hep-lat].
- [28] M. Luscher and P. Weisz, Commun. Math. Phys. **97**, 59 (1985), [Erratum: Commun. Math. Phys. 98, 433 (1985)].
- [29] M. Luscher and P. Weisz, Phys. Lett. **158B**, 250 (1985).
- [30] M. G. Alford, W. Dimm, G. P. Lepage, G. Hockney, and P. B. Mackenzie, Phys. Lett. **B361**, 87 (1995), arXiv:hep-lat/9507010 [hep-lat].
- [31] F. D. R. Bonnet, D. B. Leinweber, A. G. Williams, and J. M. Zanotti, Phys. Rev. **D65**, 114510 (2002), arXiv:hep-lat/0106023 [hep-lat].
- [32] J. Kim, W. Lee, and S. R. Sharpe, Phys. Rev. **D83**, 094503 (2011), arXiv:1102.1774 [hep-lat].
- [33] J. Kim, W. Lee, and S. R. Sharpe, Phys. Rev. **D81**, 114503 (2010), arXiv:1004.4039 [hep-lat].

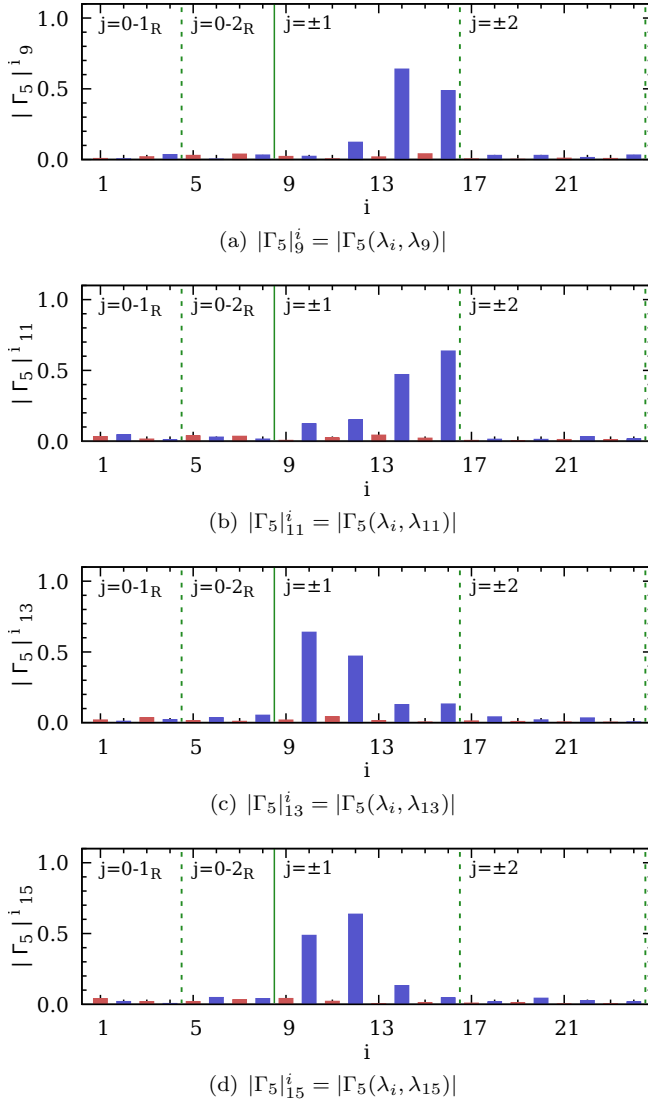


FIG. 23. $[\gamma_5 \otimes 1]$ leakage pattern for the first quartet of non-zero modes at $Q = -2$.

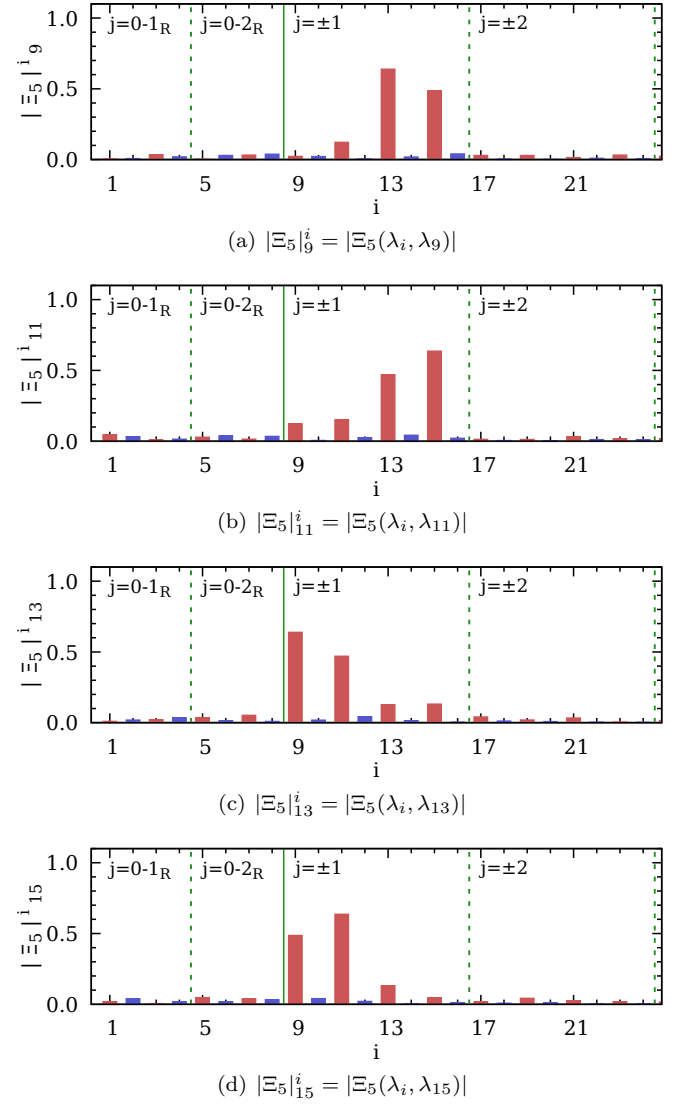
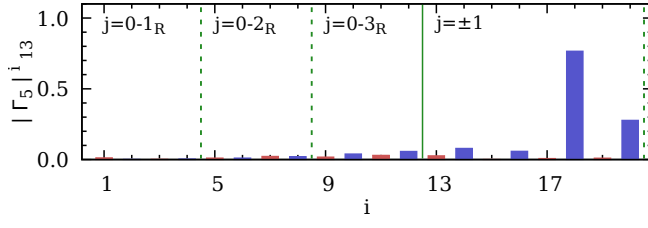
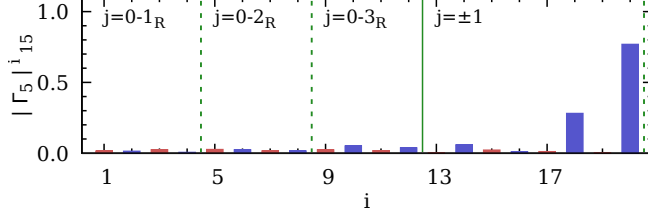
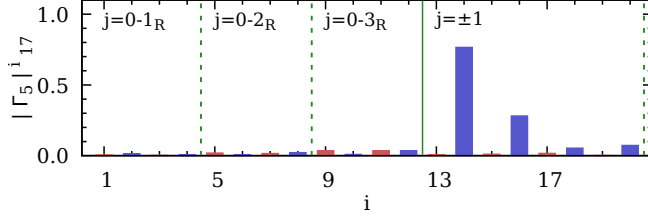
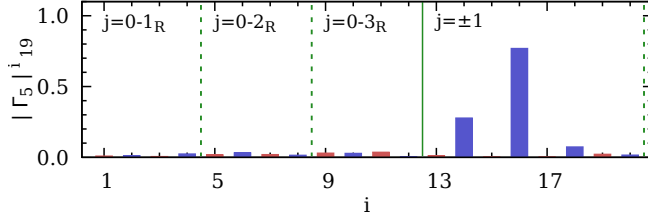


FIG. 24. $[1 \otimes \xi_5]$ leakage pattern for the first quartet of non-zero modes at $Q = -2$.

- [34] P. de Forcrand *et al.*, Nucl. Phys. **B499**, 409 (1997), arXiv:hep-lat/9701012 [hep-lat].
- [35] P. de Forcrand *et al.*, Nucl. Phys. Proc. Suppl. **47**, 777 (1996), arXiv:hep-lat/9509064 [hep-lat].
- [36] K. Cichy *et al.*, PoS **LATTICE2014**, 075 (2014), arXiv:1411.1205 [hep-lat].
- [37] A. Hasenfratz and C. Nieter, Phys. Lett. **B439**, 366 (1998), arXiv:hep-lat/9806026 [hep-lat].
- [38] M. Falcioni, M. L. Paciello, G. Parisi, and B. Taglienti, Nucl. Phys. **B251**, 624 (1985).
- [39] G. C. Donald, C. T. H. Davies, E. Follana, and A. S. Kronfeld, Phys. Rev. **D84**, 054504 (2011), arXiv:1106.2412 [hep-lat].
- [40] M. F. L. Golterman, Nucl. Phys. **B273**, 663 (1986).
- [41] M. F. L. Golterman, Nucl. Phys. **B278**, 417 (1986).
- [42] D. Verstegen, Nucl. Phys. **B249**, 685 (1985).
- [43] I. Goodfellow, Y. Bengio, and A. Courville, (MIT Press, 2016) <http://www.deeplearningbook.org>.
- [44] F. Chollet *et al.*, <https://keras.io> (2015).
- [45] D. P. Kingma and J. Ba, (2014), arXiv:1412.6980 [cs.LG].
- [46] H. Jeong, S. Lee, and W. Lee, In preparation.
- [47] Y. Aoki *et al.*, Phys. Rev. **D78**, 054510 (2008), arXiv:0712.1061 [hep-lat].
- [48] C. Sturm, Y. Aoki, N. H. Christ, T. Izubuchi, C. T. C. Sachrajda, and A. Soni, Phys. Rev. **D80**, 014501 (2009), arXiv:0901.2599 [hep-ph].
- [49] R. Lehoucq and D. C. Sorensen, SIAM J. Matrix Anal. Appl **17**, 789 (1996).
- [50] Y. Saad, Math. Comp. **42**, 567 (1984).
- [51] J. Cullum and R. Willoughby, Journal of Computational and Applied Mathematics **s 1213**, 3760 (1985).
- [52] J. Cullum and R. A. Willoughby, Journal of Computational Physics **44**, 329 (1981).
- [53] J. Cullum and R. Willoughby, Classics in Applied Mathematics **I** (2002), 10.1137/1.9780898719192.
- [54] M. A. Clark, C. Jung, and C. Lehner, EPJ Web Conf. **175**, 14023 (2018), arXiv:1710.06884 [hep-lat].

(a) $|\Gamma_5|_{13}^i = |\Gamma_5(\lambda_i, \lambda_{13})|$ (b) $|\Gamma_5|_{15}^i = |\Gamma_5(\lambda_i, \lambda_{15})|$ (c) $|\Gamma_5|_{17}^i = |\Gamma_5(\lambda_i, \lambda_{17})|$ (d) $|\Gamma_5|_{19}^i = |\Gamma_5(\lambda_i, \lambda_{19})|$ FIG. 25. $[\gamma_5 \otimes 1]$ leakage pattern for the first quartet of non-zero modes at $Q = -3$.

[55] Y.-C. Jang and C. Jung, PoS **LATTICE2018**, 309 (2019).

[56] M. Luscher, JHEP **07**, 081 (2007), arXiv:0706.2298 [hep-lat].

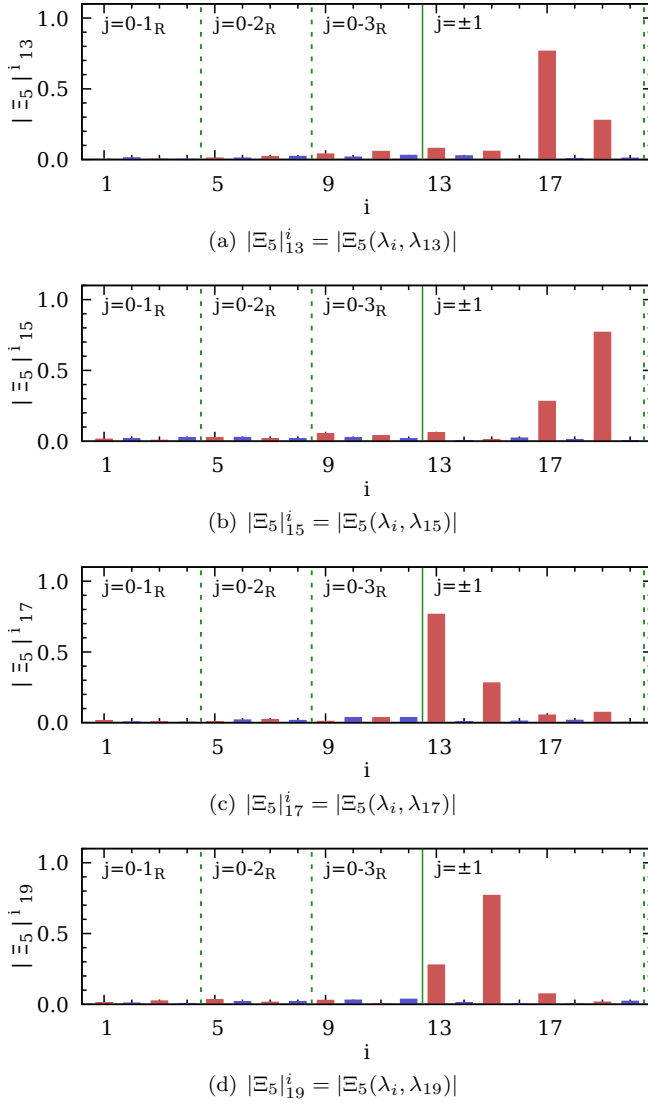


FIG. 26. $[1 \otimes \xi_5]$ leakage pattern for the first quartet of non-zero modes at $Q = -3$.